Analytical Foundation of Single-Flowpath Hypersonic RDE with Diverging Ram Inlet and Compressor

Sean H. Wang*
Wang Flight Systems Research Division LLC, Bethesda, MD†

The takeoff to cruise process of a hypersonic aircraft almost always utilizes a discrete mode transition system. A different architecture consisting of a Rotating Detonation Engine, Diverging Ram Inlet, and rim-driven feathering compressor is proposed as a mode-transition-free alternative. A quasi-1D state vector and operator formalism is derived and used to analytically model the internal flowpath at discrete component stations and calculate performance metrics as a function of Mach number, altitude, and combustor equivalence ratio. Tangential velocity is handled as a transported quantity rather than a distinct dimension. The Diverging Ram Inlet is fixed-geometry, leveraging a Mach blindspot property to preclude inlet unstart. The rim-driven compressor feathers to zero blade metal angle above Mach 3, becoming aerodynamically transparent. A series of studies investigates the model-calculated performance metrics: Theoretical specific impulse exceeds 5000s across the full envelope within the design thermal limit, and theoretical pressure recovery is 55% at Mach 5. Sensitivity analysis bounds induced velocity uncertainty to sub-unitary. This is an analytical foundation, and future experimental work will ground the architecture in measured performance data.

Nomenclature

(Nomenclature entries should have the units identified)

A	=	cross-sectional area [m^2]
A^*	=	critical choked area [m^2]
alt	=	altitude [m]
AFR	=	air-to-fuel ratio [-]
c_p	=	specific heat capacity at constant pressure [J/(kg · K)]
D_{CJ}	=	Chapman-Jouguet detonation wave velocity [m/s]
F_m	=	momentum thrust [N]
g_0	=	standard gravitational acceleration (9.81) [m/s^2]

*Contact: swang3240@gatech.edu
†Pending formation June 2026. Relocating to Atlanta, GA August 2026.

H = height [m]

h = enthalpy [J/kg]

I_{sp} = specific impulse [s]

LHV = lower heating value [J/kg]

M = Mach number [-]

$\dot{m}$ = mass flow rate [kg/s]

N = DRI module count / blade row count [-]

P = pressure [Pa]

q = specific heat addition [J/kg]

R = specific gas constant [J/(kg · K)]

r = radius [m]

T = temperature [K]

u = flow axial velocity [m/s]

v_{ax} = flow axial velocity (same as u) [m/s]

v_θ = tangential velocity [m/s]

W = width [m]

w = specific work [J/kg]

x = position [m]

$\mathbf{x}$ = flow state vector [-]

Z = blade count [-]

β_m = blade metal angle [deg]

β_s = shock angle [deg]

γ = specific heat ratio [-]

θ = flow turning angle [deg]

κ = divergence ratio [-]

π = total pressure ratio [-]

ρ = density [kg/m^3]

σ = slip factor [-]

ϕ = equivalence ratio [-]

ω = rotational velocity [rad/s]

Subscripts

0 = stagnation (axial only)

1-9	=	flowpath index
∞	=	freestream condition
i	=	input
e	=	exit
$+$	=	supersonic
$-$	=	subsonic
$*$	=	critical choked condition
t	=	total (axial and circumferential components)
$0, t$	=	stagnation (both components) (both subscripts must be invoked)

I. Introduction

A. Overview

Achieving reliable hypersonic cruise flight would fundamentally shape transcontinental travel, reducing civilian flight durations from twenty hours to two and enabling direct routes between any city pair in the world. Over the years, governments and research entities have made major advances in the field of hypersonics, the X-43A's ten-second flight [1, 2] being a historically significant example. The state of the art for hypersonic propulsion is the scramjet and the ramjet. Scramjets perform supersonic combustion under hypersonic inlet conditions [3], while ramjets operate around Mach 2-4, capped by normal shock stagnation pressure losses at Mach 6 [4]. Neither the scramjet nor the ramjet operate in subsonic or transonic conditions.

B. Literature Review

The turbofan dominates subsonic and low-supersonic flight up to approximately Mach 2, [5, 6], with the geared turbofan as the state of the art [7]. Because the turbofan operates where the ramjet cannot, in the low speed regime, this motivates the development of combined-cycle architectures. The most common is the Turbine-Based Combined Cycle (TBCC), where a discrete mode transition event within Mach 2-3 rearranges the inlet geometry to route the flow across two different systems in the integrated engine [8]. Successful TBCC inlets have been developed with bleed slots and variable geometry ramps and have been demonstrated computationally [9] and experimentally [10], covering the Mach 0-4 envelope. However, there are documented failure modes, including inlet unstart, thrust dip, and aerodynamic instability [8], and full-scale validation on a crewed vehicle remains undemonstrated [11]. Another type of combined cycle is the Rocket-Based Combined Cycle, where an ejector rocket entrains mass flow in the low-speed regime. RBCC architectures have been successfully demonstrated in the Aerojet Strutjet without causing inlet unstart [12], though oxidizer and cryogenic system mass penalties remain.

A propulsion architecture of more recent interest is the Rotating Detonation Engine (RDE). Unlike the deflagration-based combustors used in most aerospace applications, detonation couples a shock wave with heat addition. In an RDE, the detonation shock wave rotates around an annular combustor, sustained by axial injection of fresh reactants from one end [13]. This thermodynamic cycle is known as the Humphrey Cycle, and it differs from the deflagration-based Brayton Cycle. The Humphrey Cycle approaches a constant-volume process. The rotating detonation wave compresses and reacts incident gases faster than they can expand, producing a rise in both static and stagnation pressure. This is unlike the Brayton Cycle, which approaches a constant-pressure process and depletes stagnation pressure [14].

The RDE is nascent relative to the extensive history of scramjet development, with the primary focus of the literature on maintaining a stable detonation wave. Wang et al. demonstrated self-sustaining rotating detonation with non-premixed ethylene in Mach 2 conditions [15], and Meng et al. tested liquid kerosene in Mach 4 conditions across multiple equivalence ratios. Detonation wave propogation velocity was approximately 60% of the ideal Chapman-Jouguet value, with the deficit attributed to incomplete mixing, lateral relief losses, and boundary layer effects [16]. Numerical simulations have demonstrated that propulsion performance is most dependent on injection conditions rather than axial chamber length [13]. Simulations of Hydrogen-based RDEs found that simulated detonation velocities approached the ideal Chapman-Jouguet velocity better than hydrocarbon fuels [17–19], with Zheng et al.'s [18] simulation returning a 8% deficit under non-premixed viscous conditions. The computational literature furthermore characterizes RDE results adjacent to combustion. Hou et al. [20] reported time-averaged wall heat flux consistent with thermal penetration correlations, $\delta \propto \sqrt{\alpha \, \Delta t}$ and wall response to time-averaged temperature loading, not instantaneous detonation temperatures. Wu et. al. [21] investigated the isolator in an RDE ramjet configuration at Mach 2.5, identifying a critical pressure ratio below which the shock train remains stable at $\phi = 0.7$.

The rotating detonation engine has been demonstrated across propulsion classes. It has been demonstrated in rocket configurations, such as Stechmann et al.'s liquid methane RDE at Purdue University's Zucrow Laboratories [22]. In the airbreathing domain, Zhao et el. [23] presents a loose-coupling CFD framework that reports theoretical Isp values on the order of 5000 s. Ji et al. [24] presents thermodynamic parametric analysis on a RDE-based combined cycle engine, with RDE units in place of deflagration combustors for both the turbofan and ramjet. The result was a reduced minimum mode transition Mach number to 2.0, compared to 2-3 for a conventional TBCC, narrowing the thrust gap during mode transition [24].

The literature review has established the reliability of the RDE in multiple operating conditions, and as part of rockets or airbreathing engines. However, a foundational gap still remains. In airbreathing engines, the RDE is integrated as a component within combined-cycle architectures, and mode transition is treated as an engineering problem to be managed. Investigations on whether discrete mode transition can be eliminated entirely are comparatively scarce. This paper proposes an RDE-based single-flowpath architecture across the full Mach envelope with no discrete mode transition event.

C. Present Work

The present work proposes two augmentation systems not standard in the combined-cycle literature - a Diverging Ram Inlet (DRI) and a rim-driven feathering compressor. They are installed sequentially, such that each component is aerodynamically transparent when out of the operating range. This is a natural handoff. No mechanical switching or flowpath re-routing is proposed.

The DRI is a rectangular fixed-geometry inlet with multiple "modules" in sequence, each one consisting of a diverging section and a constant-area section housing a Disturbance Diamond, a streamlined body at incidence angle θ that generates an incident and reflected oblique shock. Diverging sections slightly expand the flow to counter contraction-based unstart risk without bleed slots. Enough modules are staged to drive the flow to subsonic conditions. In subsonic freestream, the DRI reduces to a plain diverging diffuser. Splitter plates divide the inlet into parallel chanels, keeping oblique shock horizontal span geometrically manageable.

The DRI discharges through a rectangular-to-annular transition diffuser, which occurs entirely in subsonic flow, into the rim-driven compressor. Torque is applied through electromagnetic rim drive, and the central shaft houses feathering servos to change the blade metal angle. Blade cross sections are streamlined half-bodies with no twist. At low speed, rotor blade metal angles induce mass flow, and the angle drops to zero as ram mass flow becomes sufficient. Eventually, rotation ceases entirely when the diverging inlet generates sufficient compression. By this point, the blades are thin simply supported beams in subsonic flow, which can be considered perturbations rather than major disturbances.

The compressor discharges into one or more annular rotation detonation chambers, each sustaining a continuous rotating hydrogen detonation wave, consistent with the literature, which demonstrated that H2 achieves closer to ideal combustion than hydrocarbons. This is followed by an aerospike converging-diverging (C-D) nozzle. Unlike an bell nozzle, an aerospike nozzle uses the ambient pressure field as a "virtual wall", which is functionally equivalent to a standard C-D nozzle with adaptive area. Exhaust expands along the aerospike ramp surface through Prandtl-Meyer waves and the plume boundary adjusts to match ambient pressure at every altitude [25]. A truncated spike recovers within 1.2% of full-length Isp with reduced length and weight [25], which is something to consider in future experimental work. The only variable-geometry component is the iris outer part of the nozzle converging section, which expands the flow to the critical sonic throat. Everything else is fixed geometry.

The paper presents a first-principles quasi-1D analytical model of the described architecture to investigate its worthiness for further experimentation. Should the architecture achieve theoretical thrust and specific impulse meeting or exceeding the Isp > 5000 s benchmark of Zhao et al. [23] across the full Mach 0 to 10 envelope, the hypothesis will be deemed met. It is important to note that this study does not claim a built architecture with validated performance metrics. This work is merely the analytical foundation. If and only if there is an analytical foundation, then future experimentation may work towards achieving full-envelope mode-transition-free hypersonic propulsion.

II. Theoretical Framework

The first step to any airbreathing propulsion is an analytical characterization. In the early stage, the question is not yet to characterize viscous and turbulent effects. It is to investigate whether the Navier-Stokes equations in the main flow direction return an engineering-worthy solution. The authors currently do not have access to experimental facilities and high-performance computing infrastructure either. It is therefore most appropriate to establish the foundation first. The present work is therefore purely analytical.

This Theoretical Framework section establishes the mathematical formulation that will be applied throughout the remainder of the paper. Rather than repeatedly applying the governing equations across a large number of subscripts, a series of mathematical operators are defined to abstract the flow relations. These operators will be applied to a flow state vector, akin to Dynamical Systems formalisms. Some of the nomenclature is not standard in the literature. Each operator maps an inlet flow state to an outlet flow state of the form

$$\mathbf{x_2} = \mathcal{F}\,\mathbf{x_1} \tag{1}$$

where $\mathbf{x}$ is the flow state vector:

$$\mathbf{x} = \begin{bmatrix} M \\ P \\ T \\ \rho \end{bmatrix} \tag{2}$$

These operators will then be assembled by mathematical composition to calculate the flow state and performance metrics at the engine's exit state and after each discrete engine component. The current model fidelity does not admit continuous flowpaths for the flow properties.

A. Governing Equations

This study treats the flow as quasi-1D ($\partial/\partial r = 0$ and $\partial/\partial\theta = 0$), steady ($\partial/\partial t = 0$), inviscid ($\mu = 0$), and calorically perfect ($d\gamma/dT = 0$ and $dc_p/dT = 0$). The governing equations are derived from reduction of the Navier-Stokes equations, presented here:

$$\rho u A = \dot{m} = \text{const} \tag{3}$$

$$\rho u \frac{du}{dx} = -\frac{dP}{dx} \tag{4}$$

$$\rho u \frac{dh}{dx} = u\frac{dP}{dx} + \dot{Q}''' \qquad [\mathrm{W/m^3}] \tag{5}$$

Conversion to stagnation properties (explained in Sec. II.B), integration of the energy equation (5) across volume, and dividing by mass flow rate yields a specific energy form,

$$c_p \Delta T_0 = q, \tag{6}$$

where q is the specific heat addition in J/kg.

Circumferential velocity is then introduced as a transported term, rather than as another dimension. This is a reduced-order approach and acknowledges that the geometric coupling terms are neglected. Nevertheless, circumferential velocity is zero in most places, excluding the compressor and the nozzle. It is not needed by most of the operators, which only act on the flow in the axial component. It is only needed in the internals of the Turbomachinery operator. This is why it is not part of flow state vector $\mathbf{x}$. The Reynolds transport equation for circumferential velocity is then

$$\rho u \frac{dv_\theta}{dx} = S_\theta \tag{7}$$

where S_θ is a production term. Following the later section highlighting the turbomachinery model (Section IV), it can be determined that S_θ is a sum of implicitly-calculated Dirac Delta functions at the area-weighted meanline radius r_m; integration would yield v_θ discretely jumping across blade rows, alternating between nonzero and zero values, and held constant otherwise. The detonation model would also create another discrete jump in v_θ.

B. Mach Number and Stagnation Properties

The Mach number is the ratio of the flow speed to the local sound speed, defined as

$$M = u/\sqrt{\gamma R T} \tag{8}$$

Unless stated otherwise, M and "Mach Number" correspond to the *axial* component of the flow. Conversely, the *total* Mach number M_t includes the circumferential component.

The Stagnation Relations model the effect of isentropically bringing the flow to rest with only applied work. These are notated as:

$$S_T(M) = \frac{T_0}{T} = 1 + \frac{\gamma - 1}{2} M^2 \tag{9}$$

$$S_P(M) = \frac{P_0}{P} = \left(1 + \frac{\gamma - 1}{2} M^2\right)^{\frac{\gamma}{\gamma - 1}} \tag{10}$$

$$S_\rho(M) = \frac{\rho_0}{\rho} = \left(1 + \frac{\gamma - 1}{2} M^2\right)^{\frac{1}{\gamma - 1}} \tag{11}$$

$$h_0 = h + \frac{1}{2}u^2 \tag{12}$$

This paper's definition of "Stagnation [PROPERTY]" $[X]_0$ only covers the deceleration of the axial component. "Total $[X]_0$" ($[X]_{0,t}$) includes the circumferential component's deceleration. This is consistent with the "v_θ-as-transport" philosophy and ensures the quasi-1D relations work as intended without violating the coordinate independence of flow velocity components. This differs from the standard convention of multidimensional compressible flow analysis, where $[X]_0$ bulks all components.

C. Isentropic Duct Operator and Area Mach Relation

Taking logarithmic derivatives of Eqs. 3, 4, 6 and eliminating intermediate variables yields an ordinary differential equation (ODE) for the axial Mach number [26, 27]:

$$\frac{dM^2}{dx} = \frac{2M^2\left(1 + \frac{\gamma-1}{2}M^2\right)}{1 - M^2}\left[-\frac{1}{A}\frac{dA}{dx} + \frac{1+\gamma M^2}{2T_0}\frac{dT_0}{dx}\right] \tag{13}$$

The $1 - M^2$ denominator vanishes at $M = 1$, representing the sonic singularity. The two bracketed terms represent area change and heat addition respectively; the equation admits flows with both mechanisms active simultaneously [28].

Within an isentropic segment $dT_0/dx = 0$ and Eq. (13) reduces to

$$\frac{dM^2}{dx} = \frac{2M^2\left(1 + \frac{\gamma-1}{2}M^2\right)}{1 - M^2}\left(-\frac{1}{A}\frac{dA}{dx}\right) \tag{14}$$

Separating variables and integrating from the throat condition $M = 1$, $A = A^*$ to an arbitrary state (M, A) recovers the Area-Mach relation (Fig. 1):

$$\int_1^{M^2} \frac{1 - M^2}{2M^2\left(1 + \frac{\gamma-1}{2}M^2\right)} dM^2 = \int_{A^*}^{A} \left(-\frac{1}{A}\right) dA \tag{15}$$

$$\frac{A}{A^*} = Y(M) = \frac{1}{M}\left[\frac{2}{\gamma+1}\left(1 + \frac{\gamma-1}{2}M^2\right)\right]^{\frac{\gamma+1}{2(\gamma-1)}} \tag{16}$$

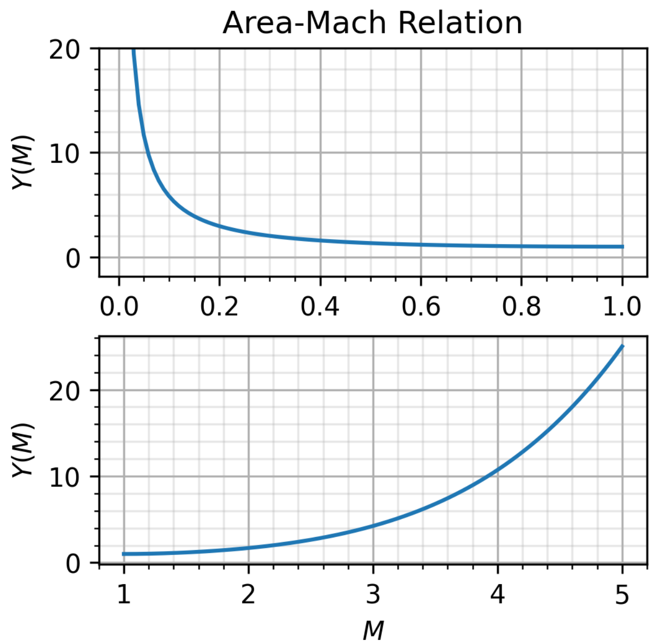

Fig. 1 Area-Mach relation $Y(M)$.

Each A/A^* value except 1 admits two Mach solutions. This motivates the definition of the subsonic and supersonic inverses, Y_-^{-1} and Y_+^{-1}. Conservation of A^* across isentropic area changes yields

$$M_2 = Y_{\mp}^{-1}\left(\frac{A_2}{A_1}Y(M_1)\right) \tag{17}$$

The Isentropic Duct Operator $\mathbf{\Phi}$ maps any inlet state to any exit state across an arbitrary isentropic area change, with stagnation properties conserved throughout and the constraint that no sonic point exists within the duct interior:

$$\mathbf{x_2} = \mathbf{\Phi}_{\mp}^{A_2 \leftarrow A_1}\,\mathbf{x_1} = \begin{bmatrix} Y_{\mp}^{-1}\left(\dfrac{A_2}{A_1}\,Y(M_1)\right) \\[2ex] P_1 \cdot \dfrac{S_P(M_1)}{S_P(M_2)} \\[2ex] T_1 \cdot \dfrac{S_T(M_1)}{S_T(M_2)} \\[2ex] \rho_1 \cdot \dfrac{S_\rho(M_1)}{S_\rho(M_2)} \end{bmatrix}, \qquad A^* \notin (A_1, A_2) \tag{18}$$

(Axial) Mach numbers are used instead of total Mach numbers. Using total Mach numbers would violate the coordinate independence of the flow when the area change and wall normal forces only apply to the axial component.

In cases where duct areas are unknown, the outlet state $\mathbf{x_2}$ can still be determined from known flow property ratios.

This is relevant for the aerospike nozzle, which expands against a virtual outer boundary rather than a physical wall. Since the exit pressure is known to equal ambient [25], the Method of Characteristics is not required to compute the endpoint state. Inverting S_P directly yields M_2, from which T_2 and ρ_2 follow. The Aerospike Operator $\mathcal{V}$, which models the effect of an aerospike nozzle is defined as

$$\mathbf{x_2} = \mathcal{V}^{P_\infty}\,\mathbf{x_1} = \begin{bmatrix} S_P^{-1}\left(\dfrac{P_1}{P_\infty}\cdot S_P(M_1)\right) \\ \\ P_\infty \\ \\ T_1 \cdot \dfrac{S_T(M_1)}{S_T(M_2)} \\ \\ \rho_1 \cdot \dfrac{S_\rho(M_1)}{S_\rho(M_2)} \end{bmatrix}, \qquad P_1 > P_\infty \tag{19}$$

The literature, including Liu et al. ([25] not [3]), has generally affirmed the aerospike nozzle performance is not significantly damaged by swirl.

D. Normal Shock Operator

A normal shock converts supersonic flow to subsonic flow non-isentropically. An ideal normal shock is a discontinuity. Discrete 1D conservation equations are used.

$$\rho_1 u_1 = \rho_2 u_2 \tag{20}$$

$$P_1 + \rho_1 u_1^2 = P_2 + \rho_2 u_2^2 \tag{21}$$

$$h_1 + \frac{1}{2}u_1^2 = h_2 + \frac{1}{2}u_2^2 \tag{22}$$

Closing with the ideal gas law and Mach number definition and solving Eqs. (20)-(22) yields the Rankine-Hugoniot relations [27, 29], collapsed here into a Normal Shock Operator mapping the pre-shock supersonic state $\mathbf{x_1}$ to the post-shock subsonic state $\mathbf{x_2}$:

$$\mathbf{x_2} = \mathbf{\Pi}\mathbf{x_1} = \begin{bmatrix} M_2 = \sqrt{\frac{(\gamma-1)M_1^2+2}{2\gamma M_1^2-(\gamma-1)}} \\ P_1\dfrac{2\gamma M_1^2-(\gamma-1)}{\gamma+1} \\ T_1\dfrac{[1+\frac{2\gamma}{\gamma+1}(M_1^2-1)](2+(\gamma-1)M_1^2)}{(\gamma+1)M_1^2} \\ \rho_1\dfrac{(\gamma+1)M_1^2}{(\gamma-1)M_1^2+2} \end{bmatrix}, \qquad M_1 > 1 \tag{23}$$

For subsonic input $M_1 \leq 1$, no shock can form and the operator reduces to the identity,

$$\mathbf{\Pi} = \mathbf{I}, \qquad M_1 \leq 1 \tag{24}$$

E. Oblique Shock Operator

Supersonic flow cannot turn against an angled disturbance without an oblique shock. This is a non-isentropic process, though the stagnation pressure loss is less than a normal shock. The Oswatitch principle states that multiple weak oblique shocks can produce an equivalent Mach change to a single strong shock with superior stagnation pressure recovery [30].

The oblique shock angle β_s, measured relative to the incoming flow direction, is related to the flow turning angle θ through the theta-beta-Mach relation [29]:

$$\tan\theta = \frac{2\cot\beta_s(M_1^2\sin^2\beta_s - 1)}{M_1^2(\gamma + \cos 2\beta_s) + 2} \tag{25}$$

This relation requires numerical solution. All physical shock angles exceed the Mach angle $\mu = \arcsin(1/M_1)$ and are bounded above by the detachment condition $d\theta/d\beta_s = 0$, which defines $\theta_{\max}$. Turning angles exceeding $\theta_{\max}$ admit no attached oblique shock solution and a detached normal shock forms instead.

The operator models the effect of a single oblique shock and not the downstream behavior. The normal Mach component upstream of the shock is

$$M_{1n} = M_1 \sin\beta_s \tag{26}$$

The normal shock operator $\mathbf{\Pi}$ is applied to the normal component:

$$\begin{bmatrix} M_{2n} \\ P_2 \\ T_2 \\ \rho_2 \end{bmatrix} = \mathbf{\Pi} \begin{bmatrix} M_{1n} \\ P_1 \\ T_1 \\ \rho_1 \end{bmatrix} \tag{27}$$

The tangential component is recovered via the tangential velocity equilibrium condition,

$$M_{2t} = M_{1t}\sqrt{\frac{T_1}{T_2}} \tag{28}$$

and the total post-shock Mach number is

$$M_2 = \sqrt{M_{2t}^2 + M_{2n}^2} \tag{29}$$

This defines the Oblique Shock Operator $\mathbf{\Gamma}^{\theta}$:

$$\mathbf{x}_2 = \mathbf{\Gamma}^{\theta}\,\mathbf{x}_1 \tag{30}$$

$$\mathbf{\Gamma}^{\theta} = \begin{cases} \mathbf{I} & M_1 < 1 \\ \mathbf{\Pi} & \theta > \theta_{\max} \end{cases} \tag{31}$$

It is acknowledged that defining an oblique shock operator, which is fundamentally an 2D phenomenon, appears at odds with a quasi-1D flow. This tension is resolved only in the context where another operator immediately undoes the turn. For a disturbance diamond, the reflected shock undoes the incident shock. Therefore, all oblique shock operators in this study appear as compositions with itself, $\mathbf{\Gamma}^{\theta}\,\mathbf{\Gamma}^{\theta}$. Under this definition, output flow will be oriented properly. The only exception is if the second oblique shock yields the normal shock branch. That results in a shock normal to its incoming flow, but looks oblique in the lab frame and exit flow will be oriented at an angle. It is therefore assumed that the post-normal-shock flow is isentropically turned back to the lab frame horizontal direction. This is acknowledged as a limitation and cannot be resolved at this fidelity. This assumption should remain generally valid if the disturbance diamond size is extremely small relative to the main duct height and the flow turning angles are small.

F. The Kantrowitz Limit

When supersonic flow encounters an area contraction, there is a risk of unstart when the back pressure exceeds a maximum limit. This expels the shock system, producing a detached bow shock and massive flow spillage [31]. The condition for self-starting follows directly from mass flow conservation. A normal shock at the inlet face produces a post-shock state $\mathbf{x_s} = \mathbf{\Pi}\,\mathbf{x_i}$, which establishes a new sonic reference area A_s^*. Isentropic contraction from the inlet area to the throat then gives $\mathbf{x_t} = \mathbf{\Phi}_{-}^{A_t \leftarrow A_i}\,\mathbf{x_s}$. If the contraction ratio $CR = A_i/A_t$ exceeds the area-Mach function evaluated at the post-shock Mach number, the throat cannot pass the required mass flow and the shock is expelled. The Kantrowitz limit for a self-starting inlet is therefore

$$\frac{A_i}{A_t} \leq Y(M_s) \tag{32}$$

where M_s is the post-normal-shock Mach number at the inlet face. A shock increases A^* by an amount scaling with stagnation pressure loss. The normal shock produces the maximum stagnation pressure loss at any freestream Mach number and therefore the most conservative Kantrowitz bound. Any oblique shock at the same Mach satisfies the limit by a wider margin automatically.

G. Detonation Combustor Operator

Fickett and Davis [32] presents a fundamental formulation that analytically models a rotating detonation as a normal shock wave moving at the ideal Chapman-Jouguet velocity D_{CJ}, coupled with specific heat addition q. The model is generally valid when the axial flow speed is slow compared to the detonation wave velocity. Since the design architecture decelerates the flow to subsonic flow regardless of freestream Mach number, this assumption is met, which bounds the errors of the fundamental detonation model.

The CJ condition requires that combustion products are sonic relative to the wave front; products cannot be supersonic without violating the entropy condition, and cannot be subsonic without an external forcing mechanism. A detailed derivation is given in Appendix A. The Chapman-Jouguet velocity is

$$D_{\mathrm{CJ}} = \sqrt{A + \sqrt{A^2 - c_1^4}}, \qquad A = c_1^2 + q(\gamma^2 - 1) \tag{33}$$

where $c_1 = \sqrt{\gamma P_1/\rho_1}$ is the reactant sound speed at the combustor inlet and q is the specific heat addition in J/kg. Under the strong-detonation approximation $P_1 \ll \rho_1 D^2$, this reduces to

$$D_{\mathrm{CJ}} \approx \sqrt{2q(\gamma^2 - 1)} \tag{34}$$

With D_{CJ} known, the post-detonation state follows from the Rayleigh-Hugoniot relations derived in Appendix A:

$$P_2 = \frac{P_1 + \rho_1 D_{\mathrm{CJ}}^2}{1 + \gamma} \tag{35}$$

$$\rho_2 = \frac{\rho_1^2 D_{\mathrm{CJ}}^2 (1 + \gamma)}{\gamma(P_1 + \rho_1 D_{\mathrm{CJ}}^2)} \tag{36}$$

Temperature follows from the ideal gas law:

$$T_2 = \frac{P_2}{\rho_2 R} \tag{37}$$

The axial velocity is unchanged by geometric argument. A shock cannot exert any force tangential to itself. Mach number changes with temperature, and the detonation combustion operator can be defined as

$$\mathbf{x_2} = \mathcal{J}^q\, \mathbf{x_1} = \begin{bmatrix} M_2 = M_1 \sqrt{T_1/T_2} \\ P_2 = \dfrac{P_1 + \rho_1 D_{\mathrm{CJ}}^2}{1 + \gamma} \\ T_2 = \dfrac{P_2}{\rho_2 R} \\ \rho_2 = \dfrac{\rho_1^2 D_{\mathrm{CJ}}^2 (1 + \gamma)}{\gamma(P_1 + \rho_1 D_{\mathrm{CJ}}^2)} \end{bmatrix} \tag{38}$$

Detonations produce swirl velocity equal to $D_{CJ} - c_2$. Since only the aerospike C-D nozzle follows this operator, and that is invariant to the non-axial component, the swirl is simply discarded unless it is needed to calculate total stagnation conditions.

The detonation operator is invariant to the scale of the combustor. One large annular chamber and multiple concentric chambers yields the same result. In practice, multiple concentric chambers is necessary by $v = \Omega r$. Fixing rotational velocity overdrives the outer wall; fixing tangential velocity shears the wave front. Beyond a critical annular gap width, both failure modes may cause the wave to extinguish.

III. Diverging Ram Inlet Model

This section covers the flowpath and modeling of the Diverging Ram Inlet. Subscripts defined in this section are local to this section.

A Diverging Ram Inlet (DRI) is a fixed-geometry inlet architecture consisting of N modules arranged in series. Each module consists of a diverging section followed by a Disturbance Diamond: a streamlined body at incidence angle θ_d that generates an incident oblique shock and its wall reflection. The diverging sections counter inlet unstart, as described in Sec. III.B.

A. Modeling Framework

A quasi-1D model for a rectangular DRI is constructed using the operators defined in Sec. II. The required parameters are the inlet width W, the initial height H_0, the per-module divergence height ΔH, the number of modules N, the Disturbance Diamond incidence angle θ_d, and the Disturbance Diamond peak height H_d. The final height follows from geometric continuity:

$$H_f = H_0 + N\Delta H \tag{39}$$

Letting $\mathbf{x}_n$ denote the flow state at the exit of the n-th module, the module recurrence relation is

$$\mathbf{x}_{n+1} = \mathbf{\Gamma}^{\theta_d}\, \mathbf{\Gamma}^{\theta_d}\, \mathbf{\Phi}_{\mp}^{(H_n+\Delta H)\leftarrow H_n}\, \mathbf{x}_n \tag{40}$$

where $H_n = H_0 + n\Delta H$ is the duct height exiting the n-th module, and $\mathbf{x}_0$ is the inlet flow state. The primary performance metric of the model is the stagnation pressure recovery across all N modules,

$$\pi = \frac{P_{0,N}}{P_{0,0}} \tag{41}$$

The model additionally verifies that the exit state $\mathbf{x}_N$ is subsonic, as required by the downstream compressor.

B. Why Diverging?

A diverging duct exhibits a Mach blindspot: for divergence ratio $\kappa = A_e/A_i$, the exit Mach number is permanently excluded from

$$M_e \notin \left(Y_-^{-1}(\kappa),\ Y_+^{-1}(\kappa)\right) \tag{42}$$

regardless of inlet condition, because area increase drives flow away from $M = 1$ on both branches. Supersonic inlet flow exits above $Y_+^{-1}(\kappa)$ and subsonic inlet flow exits below $Y_-^{-1}(\kappa)$, with both bounds moving further from unity as M_i departs from 1. No inlet perturbation can place the exit Mach number inside the blindspot interval.

The blindspot forces inlet self-starting. Any supersonic flow exiting the diverging section has Mach number at or above $Y_+^{-1}(\kappa)$. The Kantrowitz limit on the Disturbance Diamond contraction is

$$CR = \frac{H_0 + \Delta H}{H_0 + \Delta H - H_d} \leq Y(M_s) \tag{43}$$

where M_s is the post-normal-shock Mach number corresponding to pre-shock Mach $Y_+^{-1}(\kappa)$. This is verified only on the first module at pre-divergence Mach 1. Higher Mach numbers cause pre-shock Mach to be higher supersonic and post-shock Mach to be lower subsonic, increasing $Y(M_s)$. Subsequent modules have larger H_n against fixed H_d, which is a reduced contraction ratio. Therefore, verification at the first module at Mach 1 guarantees satisfaction for all DRI modules. In the subsonic input case, as long as $\Delta H > H_d$, there is no risk of choke conditions, as no point has area contract more than it has previously expanded. This is always satisfied, as the Kantrowitz limit is stricter. Divergence ratio κ should ideally be minimized with margin; large divergence ratio causes higher pre-shock Mach, which leads to more stagnation pressure loss from the same incidence angle.

C. DRI Operator

To fit the inlet into the broader operator chain, the DRI operator is defined as

$$\mathbf{x_2} = \mathcal{U}_{\mathcal{M}}\,\mathbf{x_1} = \left(\mathbf{\Gamma}^{\theta_d}\,\mathbf{\Gamma}^{\theta_d}\,\mathbf{\Phi}_{\mp}^{H_N \leftarrow H_{N-1}}\,\mathbf{\Gamma}^{\theta_d}\,\mathbf{\Gamma}^{\theta_d}\,\mathbf{\Phi}_{\mp}^{H_{N-1} \leftarrow H_{N-2}} \cdots \mathbf{\Gamma}^{\theta_d}\,\mathbf{\Gamma}^{\theta_d}\,\mathbf{\Phi}_{\mp}^{H_2 \leftarrow H_1}\,\mathbf{\Gamma}^{\theta_d}\,\mathbf{\Gamma}^{\theta_d}\,\mathbf{\Phi}_{\mp}^{H_1 \leftarrow H_0}\right)\mathbf{x_1} \tag{44}$$

where operators act right-to-left and $\mathcal{M}$ is the set of inlet modules. $\mathbf{x_1}$ and $\mathbf{x_2}$ revert to their global meaning as the inlet and exit flow states of the operator definition. Like the detonation combustor, the DRI is invariant to absolute scale, only distance-based ratios ($H_0 : \Delta H : H_d$). A single large channel and multiple parallel channels of equal total area and distance-based ratios produce the same exit state. In practice, the DRI is divided into multiple channels so the oblique shock horizontal span is geometrically manageable.

IV. Reduced-Order Turbomachinery Model

This section covers the flowpath and modeling of the rim-driven compressor. Subscripts defined in this section are local to this section.

The model operates on a single bulk flow state on the area-weighted meanline (radius r_m), consistent with the quasi-1D assumption of the broader framework. It takes the compressor inlet state as given and returns the exit state after all N blade rows ($N/2$ stages, each stage is a rotor and stator). The solver does not handle induced velocity coupling. It takes the input condition as is, processes it through all the blade rows, and assumes it is the steady state. A true iteration method to steady state requires solving an infinite-domain elliptic CFD problem, with flow-dependent source terms, which is out of scope. A sensitivity study will be conducted to evaluate the propagation of this uncertainty.

Each blade row is treated as an infinitely thin actuator disk operating at infinite blade-passing frequency. Flow properties change discretely across each volumeless blade row, corresponding to dirac delta body force terms on u and v_θ. Blade rows are assumed to be sufficiently close, such that the output of the previous blade row feeds into the input of the next blade row. Annulus area is held constant throughout the compressor. The final assumption is $\eta = 1$. Rim-driven architectures eliminate tip-clearance losses by construction, and viscosity is neglected, which is consistent with the inviscid framework throughout.

A. Local State Vector and Blade Row Direction

The turbomachinery model was created a long time before the duct operators were created; the local flow state vector is different ($\mathbf{y}$) but conversion between the $\mathbf{x}$ and $\mathbf{y}$ spaces is trivial. $\mathbf{y_{in}}$ is the inlet state; $\mathbf{y_N}$ is the exit state. The state vector is:

$$\mathbf{y} = \begin{bmatrix} T \\ v_{ax} \\ P \\ \rho \\ v_\theta \end{bmatrix} \tag{45}$$

where $v_{ax} \equiv u$ is axial velocity. v_θ is 0 at the inlet and exit states by construction.

The direction array $d_n \in \{-1, +1\}$ encodes the rotational sense of blade row n: $d_n = +1$ denotes counterclockwise rotation and $d_n = -1$ denotes clockwise rotation. For a stationary stator, the sign represents the direction of force applied to the flow. All blade row parameters are unsigned; v_θ is the sole signed quantity in the state vector. Representative stage configurations are summarized in Table 1.

Table 1 Representative stage configurations encoded by the direction array.

Configuration	N	d	ω
Single rotor	1	$[+1]$	$[\omega_r]$
Rotor-stator pair	2	$[+1, -1]$	$[\omega_r, 0]$
Counter-rotating	2	$[+1, -1]$	$[\omega_1, \omega_2]$
Two-stage with stators	4	$[+1, -1, +1, -1]$	$[\omega_1, 0, \omega_2, 0]$

B. Governing Equations

The specific work input at blade row n is given by the Euler turbomachinery equation at the area-weighted meanline radius $r_m = \sqrt{(r_{tip}^2 + r_{hub}^2)/2}$:

$$w_n = \omega_n r_m \, \Delta v_{\theta,n} \tag{46}$$

When the rotational direction changes between consecutive blade rows ($d_n \neq d_{n-1}$), the incoming swirl is reinterpreted in the reference frame of blade row n by temporarily setting

$$v_{\theta,n-1} \leftarrow -v_{\theta,n-1} \tag{47}$$

before computing $\Delta v_{\theta,n}$. This reinterpretation applies equally to rotor-rotor and rotor-stator transitions and requires no special casing. The tangential velocity change and exit tangential velocity at station n are then

$$\Delta v_{\theta,n} = -v_{\theta,n-1} + \sigma_n(\omega_n r_m - v_{ax,n-1} \tan \beta_{m,n}) \tag{48}$$

$$v_{\theta,n} = \sigma_n(\omega_n r_m - v_{ax,n-1} \tan \beta_{m,n}) \tag{49}$$

where $\sigma_n \in (0, 1]$ is the slip factor defined in Sec. IV.D and $\beta_{m,n}$ is the blade metal angle of blade row n. The ideal velocity triangle is illustrated in Fig. 2.

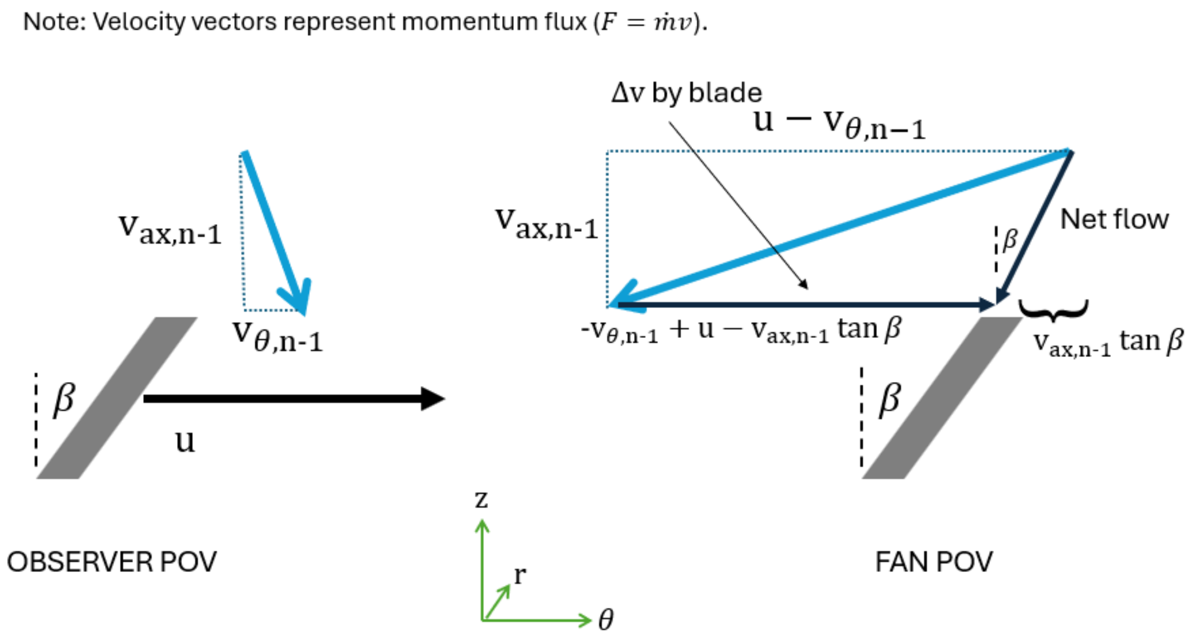

Fig. 2 Ideal rotor velocity triangle (σ = 1).

With $v_{\theta,n}$ and w_n known, the remaining 4 variables in $\mathbf{y}$ form a reduced state vector, $\mathbf{q}_n = [T_n, v_{ax,n}, P_n, \rho_n]^{\mathrm{T}}$. These are solved in a 4×4 system of energy balance, isentropic pressure rise, ideal gas law, and axial mass conservation. Defining

$$E_{\text{in}} = w_n + \frac{v_{ax,n-1}^2}{2} + \frac{v_{\theta,n-1}^2}{2}, \tag{50}$$

the system is

$$E_{\text{in}} = c_p(T_n - T_{n-1}) + \frac{v_{ax,n}^2}{2} + \frac{v_{\theta,n}^2}{2} \tag{51}$$

$$P_n = P_{n-1}\left[\frac{T_n}{T_{n-1}}\right]^{\gamma/(\gamma-1)} \tag{52}$$

$$\rho_n = \frac{P_n}{RT_n} \tag{53}$$

$$\rho_n v_{ax,n} = \rho_{n-1} v_{ax,n-1}, \tag{54}$$

with $n - 1$ = in at the first blade row.

C. Numerical Solution

The reduced state $\mathbf{q}_n$ is obtained by solving $\mathbf{R}(\mathbf{q}_n) = \mathbf{0}$, where

$$\mathbf{R}(\mathbf{q}_n) = \begin{bmatrix} E_{\text{in}} - c_p(T_n - T_{n-1}) - \dfrac{v_{ax,n}^2}{2} - \dfrac{v_{\theta,n}^2}{2} \\ P_n - P_{n-1}\left[\dfrac{T_n}{T_{n-1}}\right]^{\gamma/(\gamma-1)} \\ \rho_n - \dfrac{P_n}{RT_n} \\ \rho_n v_{ax,n} - \rho_{n-1} v_{ax,n-1} \end{bmatrix}. \tag{55}$$

The system is solved by Newton-Raphson iteration with damping factor $\alpha = 0.5$:

$$\mathbf{q}_n^{(k+1)} = \mathbf{q}_n^{(k)} - \alpha\,\mathbf{J}\left(\mathbf{q}_n^{(k)}\right)^{-1}\mathbf{R}\left(\mathbf{q}_n^{(k)}\right), \tag{56}$$

where the analytical Jacobian $\mathbf{J} = \partial\mathbf{R}/\partial\mathbf{q}_n$ is

$$\mathbf{J} = \begin{bmatrix} -c_p & -v_{ax,n} & 0 & 0 \\ -\dfrac{\gamma}{\gamma-1}\dfrac{P_{n-1}}{T_{n-1}}\left[\dfrac{T_n}{T_{n-1}}\right]^{1/(\gamma-1)} & 0 & 1 & 0 \\ \dfrac{P_n}{RT_n^2} & 0 & -\dfrac{1}{RT_n} & 1 \\ 0 & \rho_n & 0 & v_{ax,n} \end{bmatrix}. \tag{57}$$

Convergence is declared when $\|\mathbf{R}(\mathbf{q}_n)\| < 10^{-6}$, after which $v_{\theta,n}$ is appended to recover the full state $\mathbf{y}_n$.

D. Slip Factor

The slip factor σ accounts for deviation of the exit flow angle from the blade metal angle due to finite blade count. A "modified Stodola" model is employed:

$$\sigma = 1 - \frac{\pi/2}{Z} \tag{58}$$

where Z is the blade count per row. The Stodola model was originally derived for centrifugal machines with constant $C = \pi$ [33]; axial machines exhibit less slip due to the absence of the 90° flow turn, motivating the reduced constant $\pi/2$, calibrated against the axial machine data of Qiu et al. [34]. Calculating a higher-fidelity slip factor requires additional metrics about the shape of the turbomachinery and the flow conditions it faces. For a preliminary feasibility study, this is out of scope and the modified Stodola model should provide a reasonable estimate pending experimental validation.

E. Operator

The final step to close the turbomachinery model is to wrap it into an $\mathbf{x}$-space operator as part of the operator chain. Letting $\mathcal{B}$ represent the set of blade rows, the operator definition is

$$\mathbf{x_2} = \mathcal{T}_{\mathcal{B}}\, \mathbf{x_1} \tag{59}$$

Both the model input and output have no circumferential velocity. The input comes from the DRI and diffuser, which do not contribute to S_θ. The last stator ideally converts circumferential velocity to pressure, so the output has no circumferential velocity either. This allows for the map between $\mathbf{x}$ vectors and $\mathbf{y}$ vectors. Also, total stagnation properties equal stagnation properties at the endpoints.

V. Methodology

A. Operator Assembly and Computational Framework

With all the mathematical operators and internal models defined, the next step is to combine them to yield an analytical model for the design engine. Following the Present Work Section (I.C) and the operator definitions, the full operator chain evaluated right-to-left is

$$\mathbf{x_e} = \left(\mathcal{V}^{P_\infty}\, \mathbf{\Phi}_-^{A^*\leftarrow A_C}\, \mathcal{J}^{q_c}\, \mathcal{T}_{\mathcal{B}}\, \mathbf{\Phi}_-^{A_C\leftarrow A_R}\, \mathcal{U}_{\mathcal{M}}\right) \mathbf{x_1} \tag{60}$$

A cross-sectional schematic of the engine flowpath with labeled state subscripts is shown in Fig. 3. Table 2 lists the correspondence between subscripts, flowpath locations, and the operator that produced each state.

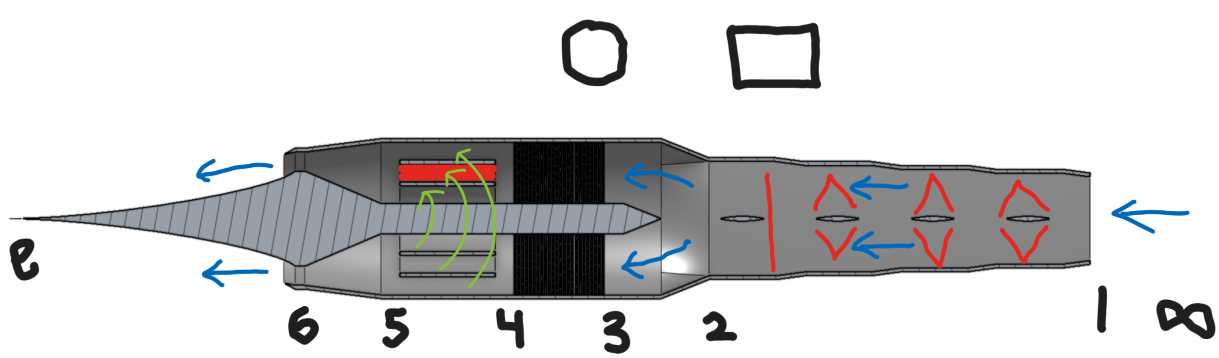

Fig. 3 Engine flowpath schematic. Grey: walls. Black: turbomachinery. Blue: flowpath. red: shocks. green: detonation wave rotation direction. Not to scale.

Table 2 Main flowpath stations and operator correspondence.

State	Description	Operator
$\mathbf{x}_\infty$	Freestream	[-]
$\mathbf{x}_1$	Inlet face	[-]
$\mathbf{x}_2$	After DRI	$\mathbf{x}_2 = \mathcal{U}_\mathcal{M}\, \mathbf{x}_1$
$\mathbf{x}_3$	After inlet-to-compressor diffuser	$\mathbf{x}_3 = \mathbf{\Phi}_-^{A_C \leftarrow A_R}\, \mathbf{x}_2$
$\mathbf{x}_4$	After compressor	$\mathbf{x}_4 = \mathcal{T}_\mathcal{B}\, \mathbf{x}_3$
$\mathbf{x}_5$	After detonation combustor	$\mathbf{x}_5 = \mathcal{J}^{q_c}\, \mathbf{x}_4$
$\mathbf{x}_6$	Nozzle throat	$\mathbf{x}_6 = \mathbf{\Phi}_-^{A^* \leftarrow A_C}\, \mathbf{x}_5$
$\mathbf{x}_e$	Nozzle exit	$\mathbf{x}_e = \mathcal{V}^{P_\infty}\, \mathbf{x}_6$

The subscripts, unlike in earlier sections, now correspond to true spatial positions within the entire engine. The engine is rectangular subscript 2 and before, and is annular subscript 3 and after.

The main computational program is an object oriented approach. The engine is an object, with geometry and operational schedules as attributes. Invoking the engine's run method requires an input of a tuple $(M_\infty, \text{alt}, \phi)$ of freestream Mach number, altitude, and combustor equivalence ratio. Each operator is its own object with a flow method, all implemented exactly with numerical inversion performed when necessary. When the engine is "run", the list of all operators is executed in order with the previous operator's output fed into the next one's input to obtain the model output - internal flow data, momentum thrust F_m, and Isp.

$$F_m = \dot{m}_{air}(u_e - u_1), \qquad I_{sp} = \frac{F_m}{\dot{m}_{fuel} \times g_0}. \tag{61}$$

Freestream states are retrieved from the US Standard Atmosphere [35]. The inlet face state $\mathbf{x_1}$ is equal to $\mathbf{x}_\infty$ unless there is induced velocity. Induction is handled in Section V.C.

B. Input Parameters

For the purposes of a feasibility study, the scale is selected for a laboratory demonstration intended for future experiments. The Diverging Ram inlet is rectangular with width $W_R = 0.75$ m, initial height $H_I = 0.44$ m ($A_I = 0.33$ m^2), and final height $H_R = 0.60$ m ($A_R = 0.45$ m^2), divided into $N = 4$ modules with per-module divergence $\Delta H = 0.04$ m. The Disturbance Diamond height is $H_D = 0.025$ m and incidence angle is $\theta_d = 12°$. This configuration was verified to satisfy the Kantrowitz criterion and to produce subsonic post-inlet flow across the full Mach 0 to 10 envelope.

The compressor and combustor share the same annular cross-section, with outer radius $r_c = 0.4$ m and shaft radius $r_{sh} = 0.08$ m ($A_C \approx 0.483$ m^2), giving a meanline radius $r_m \approx 0.288$ m. Rotors carry 17 blades ($\sigma_r = 0.907$) and stators carry 23 blades ($\sigma_s = 0.931$). The compressor consists of 12 stages ($N = 24$) of alternating rotors and stators, with a stator as the final blade row. Stators are stationary throughout with blade metal angle $\beta_m = 0$. Rotor blade metal angle and angular velocity follow the design schedules

$$\beta_m(M_\infty) = \begin{cases} 30^\circ & 0 \le M_\infty \le 0.95 \\ 0^\circ & \text{otherwise} \end{cases} \tag{62}$$

$$\omega(M_\infty) = \begin{cases} 800 \text{ rad/s} & 0 \le M_\infty \le 2 \\ 800(3 - M_\infty) \text{ rad/s} & 2 \le M_\infty \le 3 \\ 0 & \text{otherwise} \end{cases} \tag{63}$$

The detonation combustor burns H_2 with ideal lower heating value LHV = 120 MJ/kg. An effective value LHV* = 100 MJ/kg is adopted to account for dissociation losses at high combustor temperatures. The specific heat addition is

$$q_c = \text{LHV}^* \frac{\phi}{\text{AFR}} \tag{64}$$

where AFR = 34.3 is the stoichiometric air-to-fuel ratio for H_2, with nitrogen treated as inert. The fuel mass flow rate is

$$\dot{m}_{fuel} = \dot{m}_{air} \frac{\phi}{\text{AFR}} \tag{65}$$

By the nozzle throat, the central shaft has expanded to aerospike base radius $r_{sp} = 0.25$ m while the outer wall is a variable-geometry iris that maintains the sonic throat condition. All axial length parameters are treated as ideal; exact values are deferred to fabrication design and are not required by the quasi-1D framework, which is invariant to axial scale. The model computes and returns internal flow state vectors at each enumerated station, enabling trend analysis across the Mach envelope.

C. Induced Velocity and Sonic Singularities

The turbomachinery model presented in Sec. IV assumes a steady state and does not consider the induction effect. Resolving it requires solving an infinite-domain elliptical problem with a circular dependency: turbomachinery body force magnitude and flowfield properties are mutually dependent. While turbomachinery-specific computational tools exist, these are out of scope for this study. Induced velocity is therefore treated as an estimated uncertain variable requiring sensitivity study.

The magnitude of the induced velocity increment at static conditions is estimated by area-scaling a reference turbofan (GE9X) to the present inlet area, yielding $\Delta v_{ind}(0) = 100$ m/s as a conservative lower bound. For $M_\infty > 0$, the exact rate of induced velocity decrease is unknown. What's known is that above $M_\infty = 0.95$ the rotor metal angle schedule enforces $\beta_m = 0$, guaranteeing $\Delta v_{ind} = 0$. The safest approach is therefore a linear interpolation between the two known endpoints. The point estimate model is:

$$\Delta v_{ind}(M_\infty) = \begin{cases} 100\left(1 - \dfrac{M_\infty}{0.95}\right)\ \text{m/s} & 0 \le M_\infty \le 0.95 \\ 0 & \text{otherwise} \end{cases} \tag{66}$$

The inlet face velocity and Mach number are then obtained by solving the coupled system

$$u_1 = u_\infty + \Delta v_{ind}, \qquad M_1 = \frac{u_1}{\sqrt{\gamma R T_1}}, \qquad T_1 = T_\infty \frac{S_T(M_\infty)}{S_T(M_1)} \tag{67}$$

with P_1 and ρ_1 recovered from the isentropic stagnation relations, completing $\mathbf{x}_1$.

At $M_\infty = 1$, the governing equations are singular. Both sides of the Area-Mach relation are accessible and it is not clear which direction the flow takes. There are other possible effects: cowl blockage, normal shock buzz oscillation, and mixed patches of subsonic and supersonic flow; those effects cannot be resolved in a 1D model. To be conservative, the model perturbs M_∞ to the supersonic branch, which triggers the shock system and is conservative on pressure recovery.

D. Studies

With the computational model established, several studies are conducted to evaluate the first-principles theoretical performance of the RDE architecture across the Mach 0 to 10 envelope.

1. Compressor and DRI Component Performances

Study 1 evaluates the independent component performances of the compressor and the DRI over selected input conditions and schedule variation. The performance metric for both components is the total pressure ratio $\pi = P_{0,e}/P_{0,i}$ across the full component. Internal flow data is plotted discretely by blade row and inlet module for selected operating conditions.

2. Detonation Parametric Sweep and Flow Data

Study 2 conducts a large parametric sweep across the full input space $(M_\infty, \text{alt}, \phi)$ with the design geometry and schedules to characterize F_m and I_{sp} and identify performance trends across the Mach envelope. For selected operating points, internal flowfields across each operator are also plotted to isolate the contribution of each component to the overall flow evolution.

3. Compressor and DRI Performance Contributions

Study 3 isolates the performance contributions of the compressor and DRI across three operating regions: low-speed compressor-dominated, Mach 2 to 3 transition, and high-speed ram-dominated. A 2×2 factorial is conducted in the transition region and 1×2 factorials in the low- and high-speed regions. All geometries and schedules remain at design.

The low-speed baseline removes the compressor with the inlet unaffected. The transition and high-speed baselines replace the DRI with a normal-shock pitot inlet followed by a diverging diffuser of equal total area ratio and carry no turbomachinery; the normal shock is the only mechanism that decelerates supersonic flow to the subsonic condition required by the RDE, and a Busemann-type perfect shock train is explicitly excluded as an unrealistically favorable baseline. Since mass flow rate and fuel flow rate are identical across all configurations at each operating point, $\Delta I_{sp}/I_{sp} \equiv \Delta F_m/F_m$ and performance deltas are reported for F_m only.

4. Induced Velocity Sensitivity Study

Study 4 quantifies how deviations from the induced velocity point estimate propagate to model outputs. The sensitivity coefficient S is defined as the ratio of relative output deviation to relative input deviation,

$$S_{F_m} = \frac{\Delta F_m/F_m}{\Delta(\Delta v_{ind})/\Delta v_{ind}}, \qquad S_{I_{sp}} = \frac{\Delta I_{sp}/I_{sp}}{\Delta(\Delta v_{ind})/\Delta v_{ind}} \tag{68}$$

S_{F_m} and $S_{I_{sp}}$ are plotted across the low-speed input manifold. For selected operating points the full sensitivity curve is plotted to check for nonlinear effects and characterize model behavior under large deviations from the estimate. The turbomachinery schedules are held at the design point.

VI. Results

A. Study 1A: Compressor Performance

To investigate compressor performance in isolation, the component is decoupled from the full engine flowpath. For this isolated study, inlet velocity is treated as-is, to determine the component performance under the given input conditions, as if these are the post-induction effects. Since the performance metric is the stagnation pressure ratio $\pi_c = P_{0,\text{exit}}/P_{0,\text{in}}$, a relative quantity independent of absolute pressure, reinsertion downstream of the diverging inlet does not alter the results. The controls are sea level altitude, $u = 50$ m/s, $\omega = 700$ rad/s, and $\beta_m = 30°$.

Figure 4 shows π_c sensitivity to rotational speed, blade metal angle, and inlet velocity. Higher rotational speed trivially increases pressure ratio, while blade metal angle and inlet velocity decrease it by increasing the flow turning penalty $v_{ax} \tan\beta_m$ in the Euler work equation. Undefined regions (around $\beta_m > 70$) correspond to operating points where specific work becomes significantly negative, causing pressure to drop catastrophically. The model calculates negative static pressure and crashes, while in real life there would be boundary layer separation.

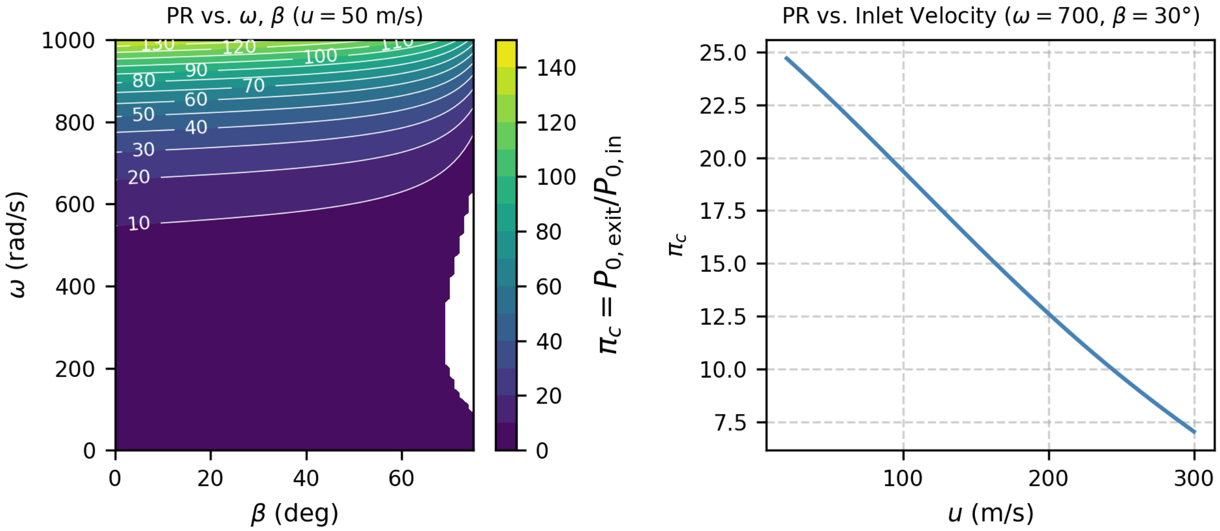

Fig. 4 Compressor π_c sensitivity to ω, β_m, and u. Non-swept variables held at control values.

Figure 5 shows the internal flow state after each blade row for a representative operating point ($u = 50$ m/s, $\omega = 700$ rad/s, $\beta_m = 30°$). Temperature rises approximately linearly through the stage sequence, consistent with nearly constant specific work input per rotor. Pressure rises nonlinearly, reflecting the isentropic relation $P \propto T^{\gamma/(\gamma-1)}$ with exponent 3.5. This plot uses *total* stagnation pressure, which steps up at each rotor and is conserved at each stator. The overall stagnation pressure ratio at this operating point is $\pi_c = 25.58$. The stagnation pressure ratio and the total stagnation pressure ratios are equal, as the exit and inlet conditions have no swirl.

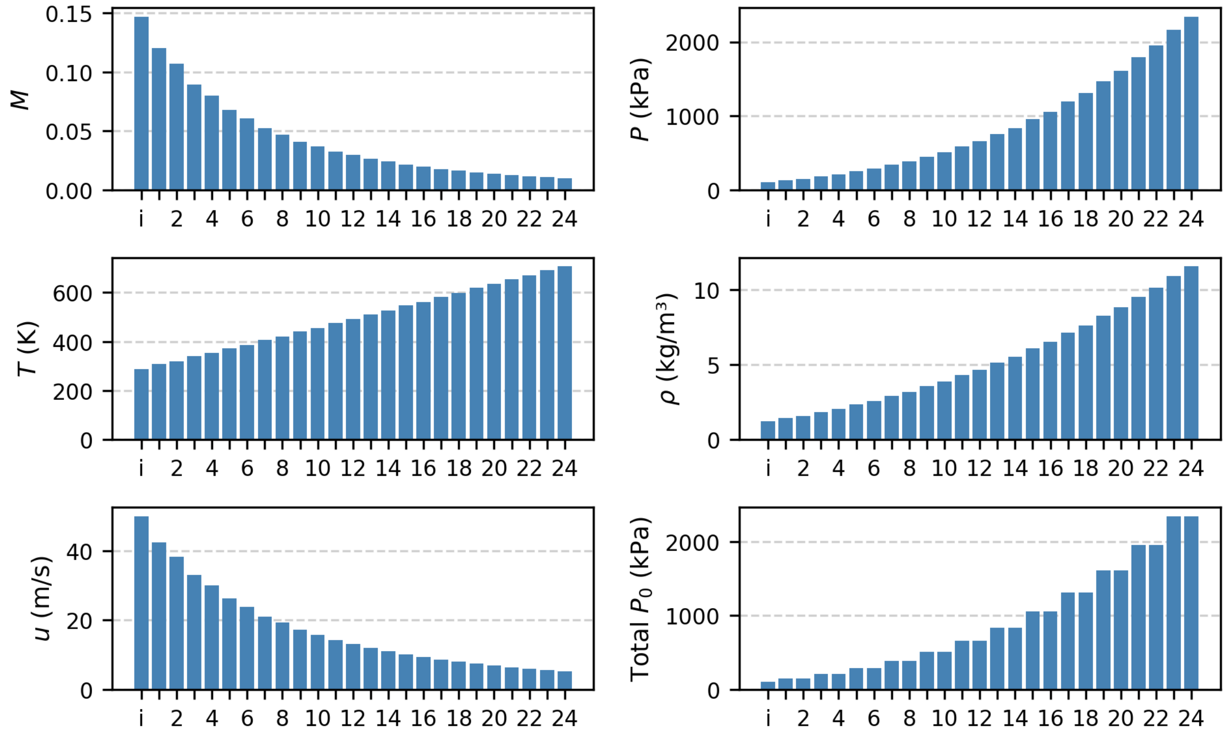

Fig. 5 Internal flow state at all blade row stations for u = 50 m/s, ω = 700 rad/s, β_m = 30°.

B. Study 1B: Diverging Ram Inlet Performance

The diverging ram inlet is evaluated in isolation across a selection of (M_∞, alt) inputs with no induced velocity. The effective module count N_{eff} denotes the number of inlet modules after which the flow has become subsonic; modules beyond N_{eff} contribute no oblique shock activity and act as plain diverging diffusers.

The first sweep characterizes the effect of shock angle on total pressure recovery. Two representative conditions are selected: M_∞ = 5, alt = 25,000 m and M_∞ = 10, alt = 30,000 m. Figure 6 presents two plots. The left panel is a Pareto curve of the best achievable pressure recovery per effective module count, achieved by tuning to the optimal shock angle and subject to a subsonic exit flow requirement. The right panel shows pressure recovery as a function of shock angle. It can be seen that effective module count decreases with increased shock angle (reduced pressure recovery). These plots reflect the oblique shock pressure loss scaling of Oswatitch [30].

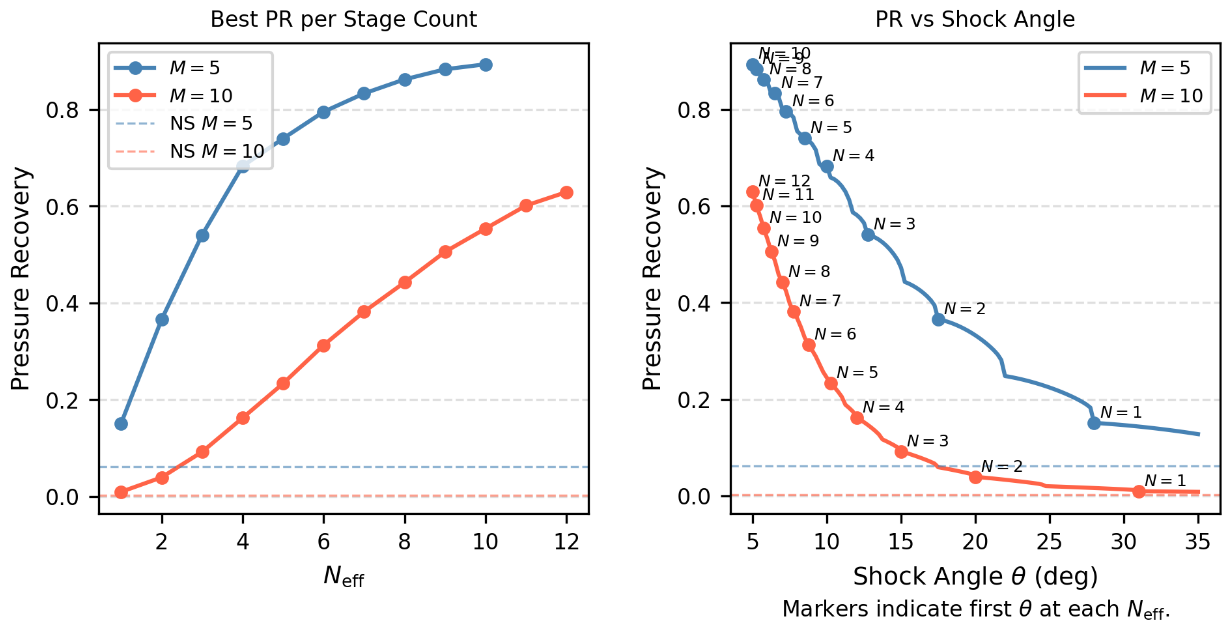

Fig. 6 Left: pressure recovery Pareto curve at optimal shock angle. Right: pressure recovery vs. shock angle across module counts.

Figure 7 presents the pressure recovery of the design inlet across the full Mach 0 to 10 envelope. The model predicts approximately 55% pressure recovery at Mach 5 and approximately 15% pressure recovery at Mach 10.

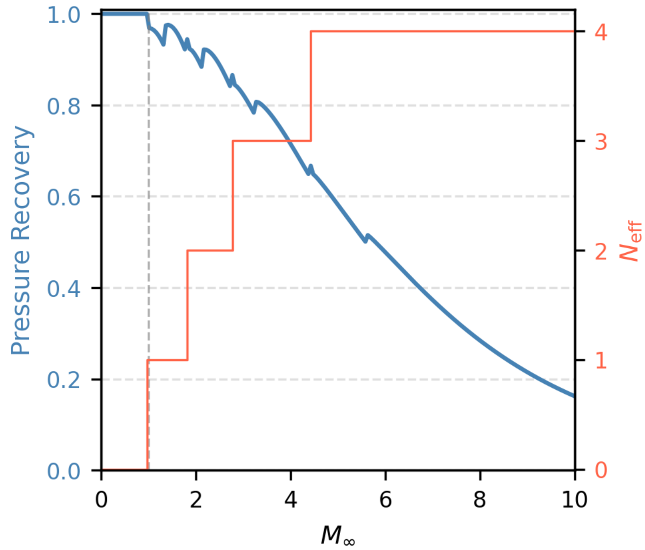

Fig. 7 Design inlet pressure recovery across the Mach 0 to 10 envelope.

Figure 8 and Figure 9 present internal flowfield metrics at all modules for two conditions, Mach 3 at 15000 m altitude and Mach 8 at 30000 m altitude. Each module contributes three discrete flow states: the diverging section exit and the two oblique shock exits. The effective module count changes as expected. Higher Mach requires more modules to decelerate the flow to subsonic given the same incidence angle. These figures use stagnation pressure not total stagnation pressure, though the absence of swirl makes both values the same.

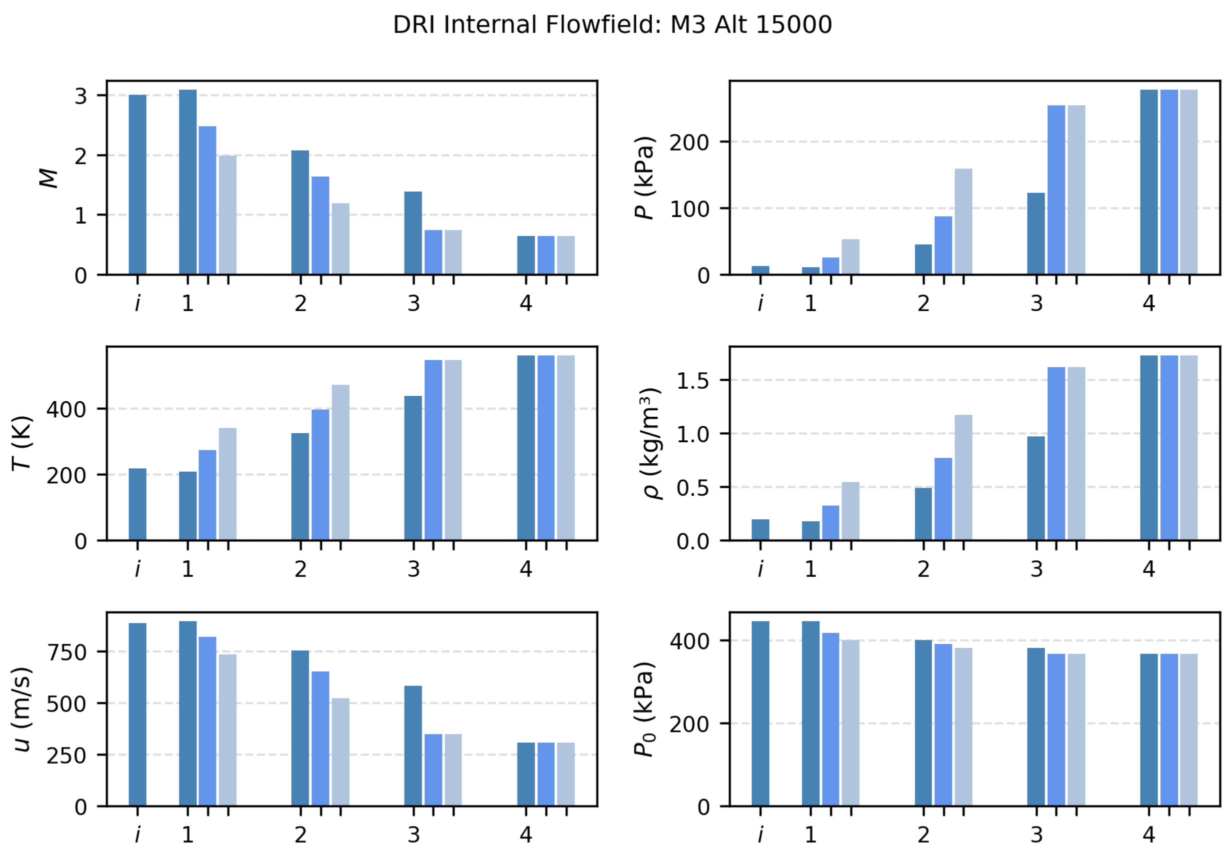

Fig. 8 Design inlet internal flowfield at $M_\infty = 3$, alt $= 15{,}000$ m. Three states per module: diverging exit and two shock exits.

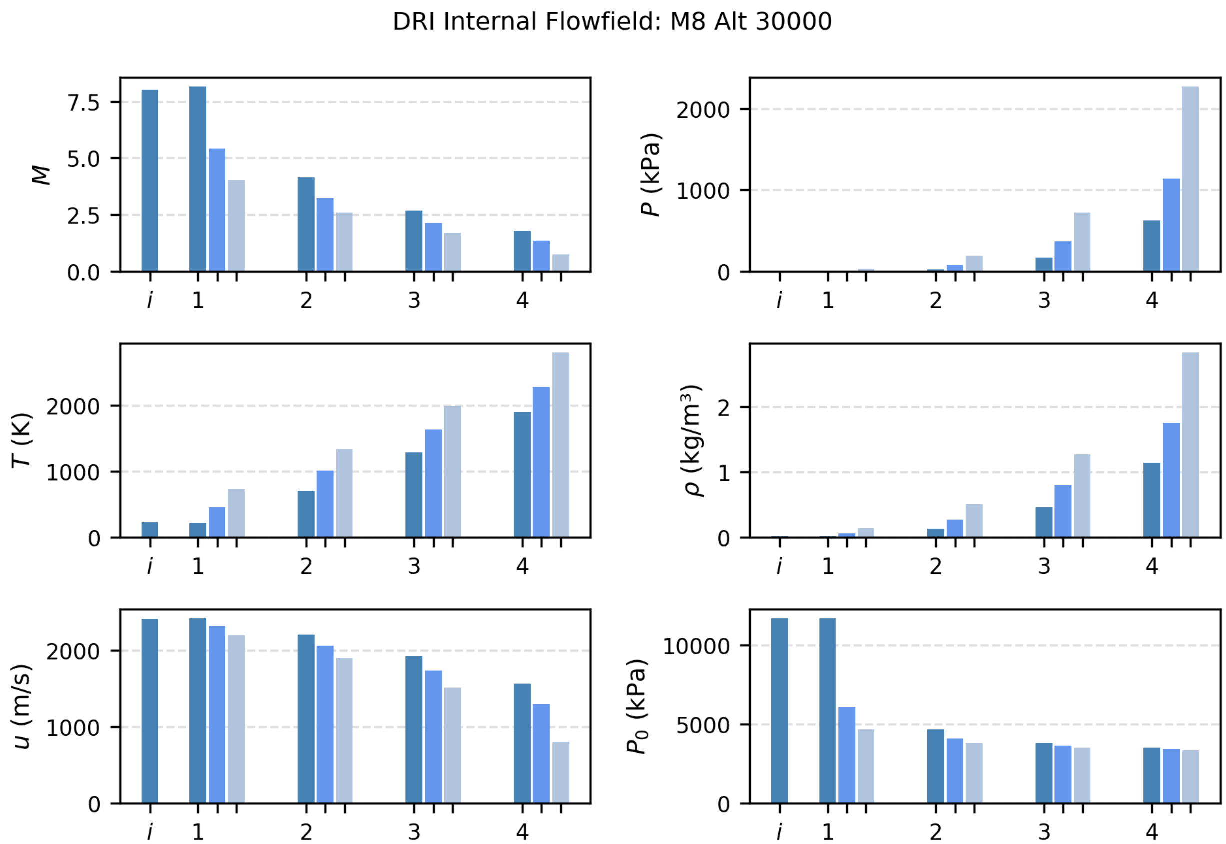

Fig. 9 Internal flowfield of the design inlet at $M_\infty = 8$, alt = 30,000 m.

C. Study 2: Detonation Parametric Sweep and Flow Data

Figure 10 presents the parametric sweep across the full input space $(M_\infty, \text{alt}, \phi)$, with altitude and ϕ discretized. Thrust increases monotonically with Mach number across all altitude levels, confirming that DRI pressure recovery more than compensates for the compressor rolloff. Specific impulse remains above the $I_{sp} > 5000$ s benchmark of Zhao et al. [23] across the bolded operating envelope for one or more ϕ curves per altitude level; bold segments indicate $T_{\text{comb}} < 6000$ K, the design thermal limit.

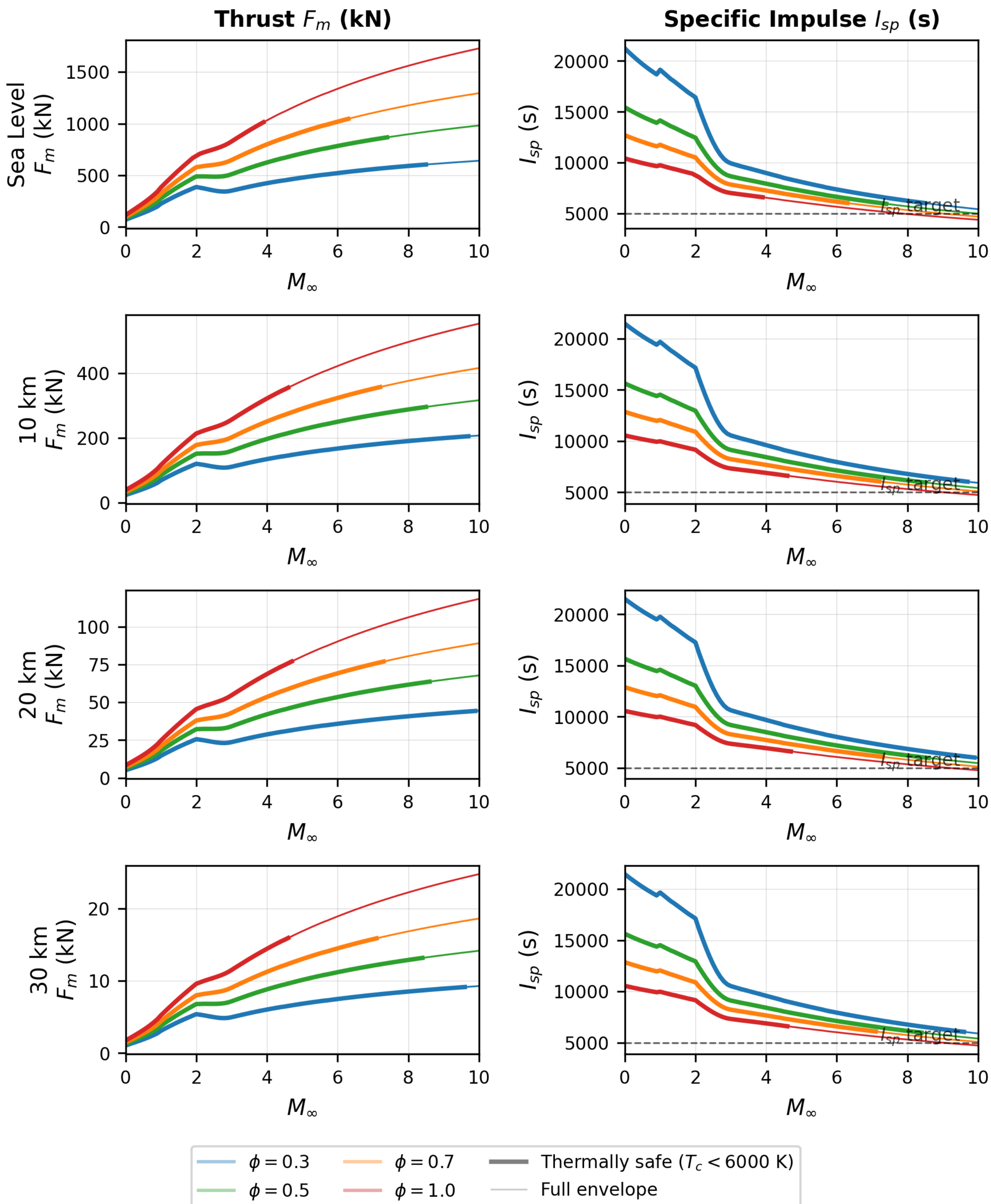

Fig. 10 Parametric sweep of F_m and I_{sp} across four altitudes and four ϕ levels. Bold segments: $T_{\text{comb}} < 6000$ K.

Four operating points are selected for internal flowfield visualization: $M_\infty = 0$ at sea level (Fig. 11), $M_\infty = 2.5$ at 10,000 m (Fig. 12), $M_\infty = 5$ at 20,000 m (Fig. 13), and $M_\infty = 10$ at 30,000 m (Fig. 14), all at $\phi = 0.5$. Station subscripts correspond to Table 2. The relative contributions of the compressor and DRI shift clearly across the four operating points, consistent with the design schedule: turbomachinery dominates at $M_\infty = 0$, both contribute comparably at $M_\infty = 2.5$, and the DRI green scatter dominates pre-combustor compression at $M_\infty = 5$ and $M_\infty = 10$. For these four figures, P_0 corresponds to stagnation pressure not total stagnation pressure. The circumferential component does NOT contribute, which means that post-detonation swirl is treated as an unrecoverable loss.

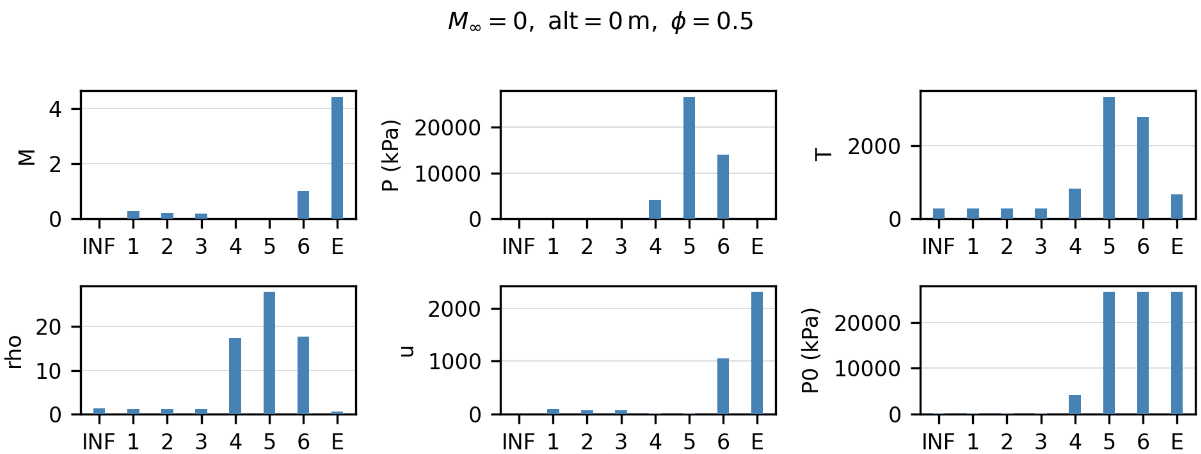

Fig. 11 Internal flowfield at $M_\infty = 0$, alt = 0 m, $\phi = 0.5$.

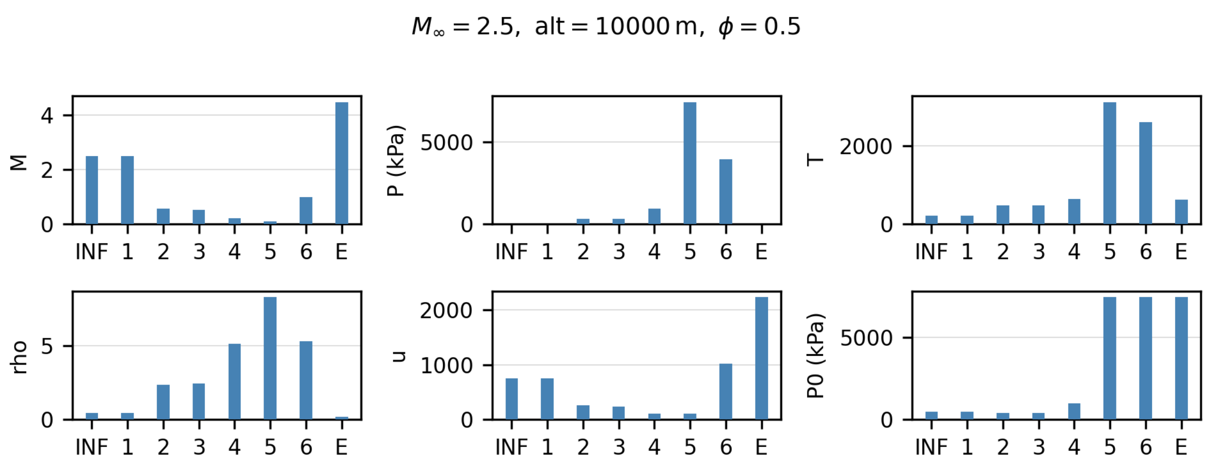

Fig. 12 Internal flowfield at $M_\infty = 2.5$, alt = 10,000 m, $\phi = 0.5$.

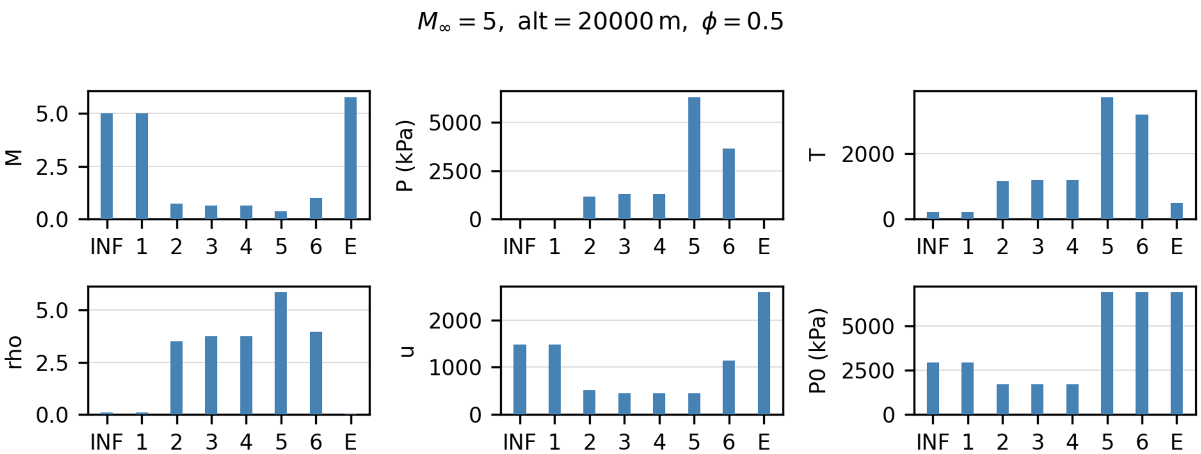

Fig. 13 Internal flowfield at M_∞ = 5, alt = 20,000 m, ϕ = 0.5.

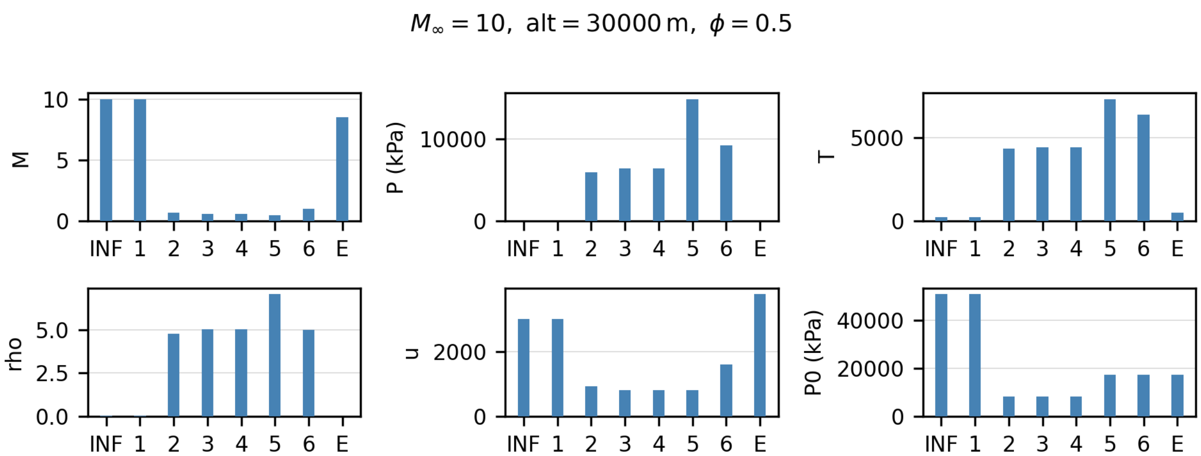

Fig. 14 Internal flowfield at M_∞ = 10, alt = 30,000 m, ϕ = 0.5.

D. Study 3: Compressor and DRI Performance Contributions

The results of Study 3 quantify the model-predicted thrust contributions of the compressor and DRI individually and in combination across three operating regions, confirming the handoff behavior established in Study 2. In the low-speed region (Table 3), the compressor delivers 31 to 38% thrust augmentation over the no-compressor baseline. In the transition region (Table 4), the crossover is directly observable by $M_\infty = 2.7$, where DRI and turbomachinery contributions have inverted relative to $M_\infty = 2.3$. In the high-speed region (Table 5), the DRI relative thrust gain increases monotonically from 12.1% at $M_\infty = 4$ to 55.5% at $M_\infty = 10$. The inlet is increasingly beneficial at higher freestream Mach, where the alternative would be catastrophic normal shock stagnation pressure loss.

Table 3 Low-speed region: compressor thrust contribution at $\phi = 0.5$, DRI active.

M_∞	alt (m)	F_{base} (kN)	F_{comp} (kN)	ΔF (kN, %)
0.5	0	123.3	168.5	+45.2 (+36.6%)
1.0	0	202.0	278.3	+76.4 (+37.8%)
1.0	5000	116.2	159.7	+43.5 (+37.4%)
1.5	5000	167.6	225.4	+57.8 (+34.5%)
2.0	5000	214.3	282.9	+68.5 (+32.0%)
2.0	10000	115.1	151.6	+36.4 (+31.6%)

Table 4 Transition region: factorial component contributions at $\phi = 0.5$.

M_∞	alt (m)	F_{base} (kN)	F_{inlet} (kN)	F_{turbo} (kN)	F_{both} (kN)	Δ(in−base) (kN, %)	Δ(turbo−base) (kN, %)	Δ(both−in) (kN, %)	Δ(both−turbo) (kN, %)
2.3	10000	125.9	129.8	149.1	152.3	+3.9 (+3.1%)	+23.2 (+18.4%)	+22.5 (+17.4%)	+3.2 (+2.2%)
2.3	15000	58.7	60.5	69.6	71.0	+1.8 (+3.0%)	+10.8 (+18.4%)	+10.5 (+17.3%)	+1.5 (+2.1%)
2.7	15000	65.6	69.0	68.2	71.5	+3.3 (+5.0%)	+2.6 (+3.9%)	+2.5 (+3.6%)	+3.2 (+4.7%)
2.7	20000	30.0	31.5	31.1	32.6	+1.5 (+5.0%)	+1.2 (+3.9%)	+1.1 (+3.6%)	+1.5 (+4.7%)

Table 5 High-speed region: DRI thrust contribution at $\phi = 0.5$, turbomachinery feathered.

M_∞	alt (m)	F_{base} (kN)	F_{DRI} (kN)	ΔF (kN, %)
4.0	20000	37.5	42.1	+4.5 (+12.1%)
5.0	25000	18.6	21.9	+3.3 (+17.7%)
6.0	25000	19.6	24.2	+4.6 (+23.5%)
7.0	30000	9.3	12.1	+2.8 (+30.8%)
8.0	30000	9.3	12.9	+3.6 (+38.1%)
10.0	30000	9.1	14.1	+5.1 (+55.5%)

E. Study 4: Induced Velocity Sensitivity Study

The sensitivity coefficient S is a normalized ratio and it quantifies dominant model uncertainty by determining whether relative input deviations cause larger or smaller relative output deviations. All results are computed at sea level and $\phi = 0.5$.

Figure 15 shows S_{F_m} and $S_{I_{sp}}$ across the low-speed Mach envelope under small perturbations. Both coefficients are sub-unitary throughout, confirming that a 1% deviation in induced velocity produces less than 1% deviation in either output. S_{F_m} peaks near $M_\infty = 0$ where induced velocity is the sole source of inlet momentum, and decays monotonically as ram pressure takes over. $S_{I_{sp}}$ is negative across the envelope and of smaller magnitude than S_{F_m}. This is because higher induced velocity increases mass flow ingestion, and fuel flow rate increases to meet $\phi = 0.5$.

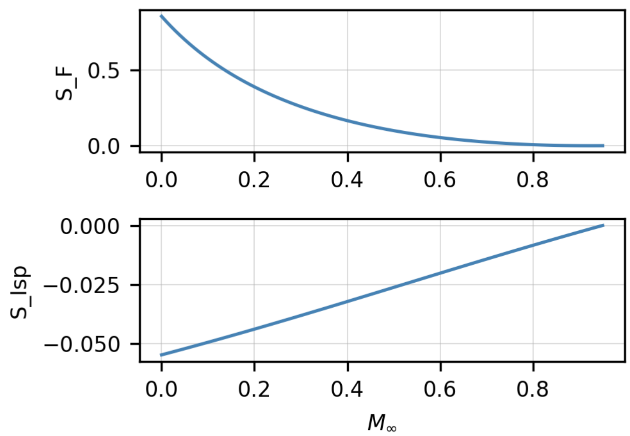

Fig. 15 S_{F_m} **and** $S_{I_{sp}}$ **across the low-speed Mach envelope. Both coefficients remain below unity throughout.**

Figures 16 and 17 extend the analysis to large perturbations of ±80% from the point estimate at $M_\infty = 0$ and $M_\infty = 0.5$ respectively. The output response is nearly globally linear with the thrust plot being concave down. This confirms that even with catastrophically erroneous predictions of induced velocity, thrust changes in a predictable manner. At $M_\infty = 0.5$, the error bands narrow, consistent with the decay of S observed in Fig. 15.

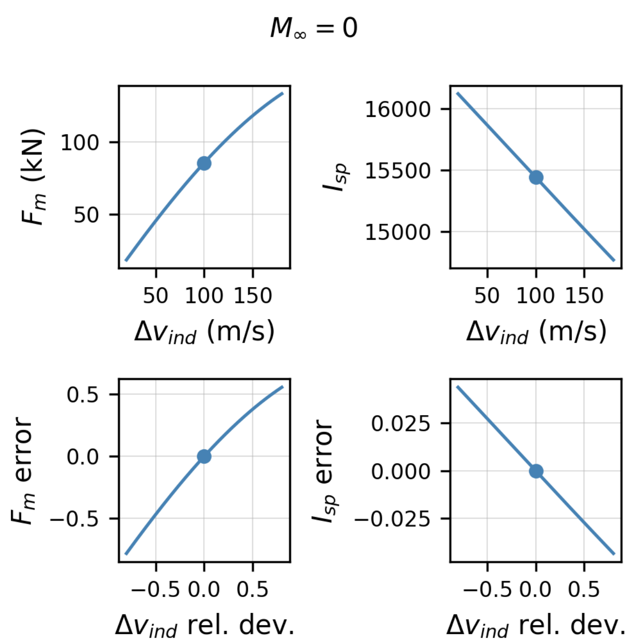

Fig. 16 F_m **and** I_{sp} **response to ±80% induced velocity perturbations at** $M_\infty = 0$**.**

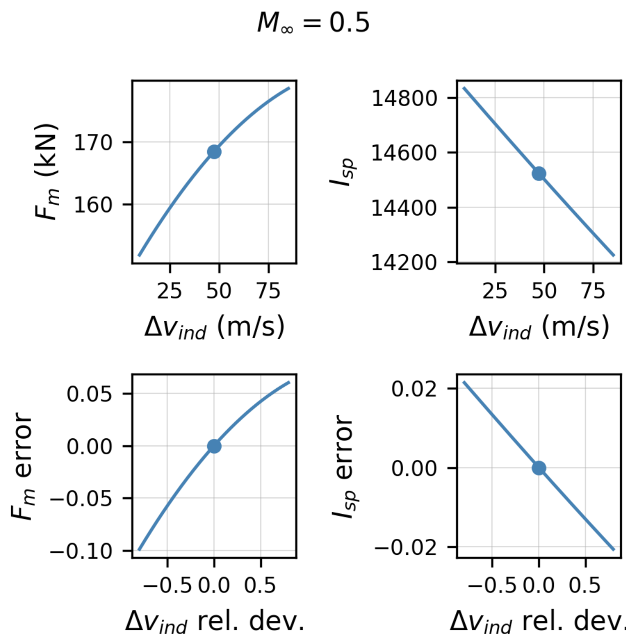

Fig. 17 F_m **and** I_{sp} **response to** $\pm 80\%$ **perturbations at** $M_\infty = 0.5$**.**

VII. Discussion

A. Meeting the Hypothesis

The parametric sweep of study 2 confirms that the hypothesis is met. An analytical quasi-1D reduced order model implemented from first-principles compressible flow relations shows that the theoretical Isp exceeds 5000 across the entire Mach envelope. Study 3 isolates the individual contributions of the compressor and DRI, demonstrating significant theoretical thrust augmentation from each component. Study 4 bounds the dominant model uncertainty: induced velocity error propagates sub-unitary and nearly linear.

Together, these results establish a potential analytical basis for the feasibility of a single-flowpath hypersonic RDE with no mode transition. These numbers would motivate future experiments to quantify the errors arising from the model assumptions. Should the experiment be successful, it could potentially contribute to fitting the gap in the literature - an engine operating across the entire Mach envelope with continuous aerodynamic handoff, not discrete mode transition.

Nevertheless, quasi-1D models serve a role that CFD cannot replicate at this program stage.They provide a reasonable *estimate* of performance and flow metrics in milliseconds, allowing for sweeping the large multidimensional input space across the Mach envelope. Attempting to design a totally distinct engine architecture and test it with CFD would be extremely computationally prohibitive and requires a reference geometry to discretize. This architecture does not yet have a reference. The quasi-1D model therefore answers the feasibility question first and identifies which regions of the input space warrant future experimentation.

B. Diverging Ram Inlet

Study 1B demonstrates the theoretical viability of the diverging ram inlet as an alternative to traditional mixed compression inlets. Applying deliberate duct divergence is not a standard practice, as the standard assumption is that flow expansion is at odds with pressure recovery. This note is acknowledged but is a feature of the inlet - the Mach blindspot property counters choking-induced inlet unstart by trading slight pressure recovery.

Another consequence of the DRI architecture is its independence from natural shock train development. Ideally, the disturbance diamonds would induce all the shocks, and the wall would induce the shock reflection. There is no dependence on an uncontrolled shock train, which may mitigate transient instability-induced unstart as long as the incident shocks remain attached. However, there will be significantly more shock-shock interactions caused by shock train overlapping. Whether they help or hurt pressure recovery is uncertain and requires investigation.

The upside is that the inlet is fixed geometry and requires no mechanical complexity across the Mach 0 to 10 envelope. The main limitation is that shallow shock angles cause horizontal distance requirement to scale following roughly $NH \cot(\beta_s)$. Without splitter plates, the horizontal span becomes extremely large, especially at higher Mach where $\beta_s \to \theta$. Splitter plates are therefore structurally necessary.

C. Rim Driven Turbomachinery

The conventional argument precluding the development of single-flowpath architectures is that turbomachinery cannot survive above Mach 3. The design architecuture has two potential responses to the standard argument. The first is that incoming flow towards the compressor is subsonic, having underwent ramjet-like (supersonic to subsonic) compression through the DRI. Shocks can no longer form, and the zero-AoA streamlined bodies allow for the use of small-disturbance or thin-airfoil theories for high-fidelity calculations. The other response is the rim-driven aspect. Rim-driven architectures transform the blades from cantilevers to simply supported. There is no tip clearance leakage. The absence of blade twist permits thicker cross-sections compatible with UHTC surface coatings and internal coolant lines to counter post-inlet temperatures. By the point temperature is significant (Mach 6+), the blades are not moving, having already stopped by Mach 3. The exact design of the rim-drive mechanism and the blade profile is up to future investigation.

The feathering schedule to zero blade metal angle across the entire blade body is not standard compressor practice. Compressor blades typically have twist. Even if they didn't, the standard practice does not feather them to zero blade metal angle. However, this non-standard practice produces a performance boost, in which Euler work is maximized following the Euler turbomachinery equation. Circumferential velocity change is at its maximum, producing the largest per-stage total pressure ratios.

The slight non-monotonicity in thrust around Mach 2 to 3 reflects the compressor schedule rather than a physical discontinuity. As the rotor feathers and spins down across this interval, its pressure contribution falls before ram recovery fully compensates, producing a local inflection. The shape is an artifact of the chosen schedule values and would be eliminated by a more refined control algorithm.

D. Combustor Structural and Thermal Requirements

The $T_{\text{comb}} < 6000$ K limit applied in Study 2 does not impose a 6000 K wall condition. The detonation wave is periodic, and experiments (like Hou et al. [20]) would show that time-averaged flux, not instantaneous peak detonation temperature, governs wall loading. The effective thermal requirement is thus expected to remain within UHTC operating range, pending experimentation.

At high combustor pressures the governing structural limit is hoop stress $\sigma = Pr/t$. Rocket combustion chambers routinely operate at tens of MPa under this same relation; the present combustor pressure envelope is less demanding. The requirement is already solved by existing practice.

E. Limitations

A few limitations have already been noted throughout the study and are consequences of using a reduced-order 1D model. The remaining ones are the following:

Viscosity is excluded at all points in the model. This is expected to impose a performance penalty. However, the governing fluid mechanics are inertia based, therefore the flow should not be destroyed entirely. As previously acknowledged, the DRI will have more shock-shock interactions, which requires future investigation.

The second limitation is calorically perfect gas. γ should decrease at high temperatures, and dissociation occurs above 3000 K. This is partially accounted for by the reduced LHV value but is otherwise not modeled in finer detail. Nevertheless, H2 has the smallest characteristic combustion time and cell size of any fuel. Combustion occurs at a shorter timescale than fluid flow. Combustion deviation from ideal should be comparatively less of a deviation than of hydrocarbon combustion.

The third limitation is in the meanline turbomachinery model. The slip factor breaks down in stators, as both angular velocity and blade metal angle are zero. $\sigma \times 0$ is still zero. This causes the modeled stators to perform isentropic total stagnation pressure recovery while minor pre-combustion swirl exists in practice. This effect is second-order relative to the first two limitations.

VIII. Conclusions

This paper developed a state vector and operator based formalism for abstraction of compressible flow relations. These formalisms were utilized to develop a reduced-order quasi-1D analytical model with swirl transport to simulate a proposed mode-transition free architecture combining a Rotating Detonation with a Diverging Ram Inlet and rim-driven feathering compressor. Simulation across the full input space from takeoff to hypersonic conditions resulted in theoretical

Isp metrics of > 5000 s and thrust on the order of 10s to 100s of kN across the Mach envelope for the design geometry. Induced velocity sensitivity effect is bounded and nearly linear. The analytical foundation is theoretically sound at the appropriate fidelity level - quantifying the feasibility and engineering worthiness. The next step is fabrication of a laboratory demonstrator and experimental validation to ground the architecture in real-world conditions.

Appendix

A. Derivation of the Chapman-Jouguet Detonation Wave Velocity

A.1: Assumptions

- The wave front is parallel to the axis (Chapman normality condition).
- The flow is inviscid throughout.
- Combustion is instantaneous and ideal, modeled by specific heat addition q per unit mass.
- The gas is ideal and calorically perfect with constant γ.
- The initial axial velocity of the reactants entering the combustor is neglected.

A.2: Conservation Equations

The wave is analyzed in the wave-fixed frame. Reactants enter at speed D and products leave at speed u_2, both measured relative to the wave. The conservation of mass, momentum, and energy across the wave front are

$$\rho_1 D = \rho_2 u_2 \tag{69}$$

$$P_1 + \rho_1 D^2 = P_2 + \rho_2 u_2^2 \tag{70}$$

$$\frac{\gamma}{\gamma - 1}\frac{P_1}{\rho_1} + \frac{D^2}{2} + q = \frac{\gamma}{\gamma - 1}\frac{P_2}{\rho_2} + \frac{u_2^2}{2} \tag{71}$$

The system is closed by the ideal gas law $P = \rho R T$ and the Chapman-Jouguet condition, which states that the products are sonic relative to the wave,

$$u_2 = c_2 = \sqrt{\gamma R T_2} = \sqrt{\frac{\gamma P_2}{\rho_2}} \tag{72}$$

A.3: Reduction to Three Equations

Substituting Eq. 72 into Eq. 69 eliminates u_2 from the mass equation,

$$\rho_1 D = \sqrt{\gamma P_2 \rho_2} \tag{73}$$

Substituting Eq. 72 into Eq. 70 eliminates u_2 from the momentum equation,

$$P_1 + \rho_1 D^2 = P_2 + \gamma P_2 = P_2(1+\gamma) \tag{74}$$

Substituting Eq. 72 into Eq. 71 and grouping the right-hand side over a common denominator $2(\gamma-1)$,

$$\frac{\gamma}{\gamma-1}\frac{P_2}{\rho_2} + \frac{1}{2}\frac{\gamma P_2}{\rho_2} = \frac{P_2}{\rho_2}\left(\frac{2\gamma + \gamma(\gamma-1)}{2(\gamma-1)}\right) = \frac{P_2}{\rho_2}\frac{\gamma(\gamma+1)}{2(\gamma-1)} \tag{75}$$

so the energy equation becomes

$$\frac{\gamma}{\gamma-1}\frac{P_1}{\rho_1} + \frac{D^2}{2} + q = \frac{P_2}{\rho_2}\frac{\gamma(\gamma+1)}{2(\gamma-1)} \tag{76}$$

A.4: Elimination of P_2 and ρ_2

Squaring Eq. 73 gives a relation between P_2 and ρ_2,

$$P_2\rho_2 = \frac{\rho_1^2 D^2}{\gamma} \tag{77}$$

Solving Eq. 74 directly for P_2,

$$P_2 = \frac{P_1 + \rho_1 D^2}{1+\gamma} \tag{78}$$

Dividing Eq. 77 by Eq. 78 gives ρ_2,

$$\rho_2 = \frac{\rho_1^2 D^2}{\gamma} \cdot \frac{1+\gamma}{P_1 + \rho_1 D^2} = \frac{\rho_1^2 D^2(1+\gamma)}{\gamma(P_1 + \rho_1 D^2)} \tag{79}$$

Dividing Eq. 78 by Eq. 79 gives P_2/ρ_2,

$$\frac{P_2}{\rho_2} = \frac{P_1 + \rho_1 D^2}{1+\gamma} \cdot \frac{\gamma(P_1 + \rho_1 D^2)}{\rho_1^2 D^2(1+\gamma)} = \frac{\gamma(P_1 + \rho_1 D^2)^2}{\rho_1^2 D^2(1+\gamma)^2} \tag{80}$$

Substituting Eq. 80 into Eq. 76,

$$\frac{\gamma}{\gamma-1}\frac{P_1}{\rho_1} + \frac{D^2}{2} + q = \frac{\gamma(P_1 + \rho_1 D^2)^2}{\rho_1^2 D^2(1+\gamma)^2} \cdot \frac{\gamma(\gamma+1)}{2(\gamma-1)} = \frac{\gamma^2(P_1 + \rho_1 D^2)^2}{2\rho_1^2 D^2(\gamma^2-1)} \tag{81}$$

A.5: Forming the Quadratic

Multiplying both sides of Eq. 81 by $2\rho_1^2 D^2(\gamma^2 - 1)$ and expanding,

$$2\rho_1^2 D^2 \gamma \frac{P_1}{\rho_1(\gamma - 1)}(\gamma^2 - 1) + \rho_1^2 D^4(\gamma^2 - 1) + 2q\rho_1^2 D^2(\gamma^2 - 1) = \gamma^2(P_1 + \rho_1 D^2)^2 \tag{82}$$

The first term on the left simplifies using $(\gamma^2 - 1) = (\gamma - 1)(\gamma + 1)$,

$$2\rho_1^2 D^2 \gamma \frac{P_1}{\rho_1(\gamma - 1)}(\gamma^2 - 1) = 2\rho_1 D^2 \gamma P_1(\gamma + 1) \tag{83}$$

Expanding the right-hand side,

$$\gamma^2(P_1 + \rho_1 D^2)^2 = \gamma^2 P_1^2 + 2\gamma^2 P_1 \rho_1 D^2 + \gamma^2 \rho_1^2 D^4 \tag{84}$$

Collecting all terms onto the left and grouping by powers of D,

$$\rho_1^2 D^4(\gamma^2 - 1 - \gamma^2) + D^2\left(2\rho_1 P_1 \gamma(\gamma + 1) - 2\gamma^2 P_1 \rho_1 + 2q\rho_1^2(\gamma^2 - 1)\right) - \gamma^2 P_1^2 = 0 \tag{85}$$

The coefficient of D^4 simplifies to $-\rho_1^2$. The coefficient of D^2 simplifies by factoring $2\rho_1 P_1 \gamma$,

$$2\rho_1 P_1 \gamma(\gamma + 1) - 2\gamma^2 P_1 \rho_1 = 2\rho_1 P_1 \gamma\left[(\gamma + 1) - \gamma\right] = 2\rho_1 P_1 \gamma \tag{86}$$

so Eq. 85 becomes

$$-\rho_1^2 D^4 + 2D^2\left(\rho_1 P_1 \gamma + q\rho_1^2(\gamma^2 - 1)\right) - \gamma^2 P_1^2 = 0 \tag{87}$$

Dividing through by $-\rho_1^2$ and substituting $P_1/\rho_1 = c_1^2/\gamma$,

$$D^4 - 2D^2\left(c_1^2 + q(\gamma^2 - 1)\right) + c_1^4 = 0 \tag{88}$$

where $c_1 = \sqrt{\gamma P_1/\rho_1}$ is the reactant sound speed.

A.6: Solution

Equation 88 is a quadratic in D^2. Defining $A \equiv c_1^2 + q(\gamma^2 - 1)$ and applying the quadratic formula,

$$D^2 = A \pm \sqrt{A^2 - c_1^4} \tag{89}$$

Taking the detonation root,

$$\boxed{D_{\mathrm{CJ}} = \sqrt{A + \sqrt{A^2 - c_1^4}}, \qquad A = c_1^2 + q(\gamma^2 - 1)} \tag{90}$$

In the limit $P_1 \ll \rho_1 D^2$, the reactant sound speed $c_1 \to 0$ and Eq. 90 reduces to the classical strong-detonation approximation,

$$D_{\mathrm{CJ}} \approx \sqrt{2q(\gamma^2 - 1)} \tag{91}$$

The exact form, Eq. 90, is retained throughout this work to preserve the dependence on compressor delivery pressure P_1 through c_1.

Funding Sources

The authors have no funding sources to declare. The research is internally self funded and fully computational.

Data Availability Statement

All codes utilized in this study are available in a private GitHub repository available upon request for academic review purposes.

Acknowledgments

There are no acknowledgments.

Conflicts of Interest

The author declares a financial interest in the subject matter of this manuscript as Founder and Director of Wang Flight Systems Research Division LLC (pending formation 6/2026), which holds commercial interest in the propulsion architecture described herein. This is an aligned, not necessarily competing interest. It is nevertheless declared for good faith.

References

[1] Voland, R. T., Huebner, L. D., and McClinton, C. R., "X-43A Hypersonic Vehicle Technology Development," Tech. Rep. IAC-05-D2.6.01, NASA Langley Research Center, 2005. 56th International Astronautical Congress, Fukuoka, Japan. Available: `https://ntrs.nasa.gov/api/citations/20050239566/downloads/20050239566.pdf`.

[2] Marshall, L. A., Corpening, G. P., and Sherrill, R., "A Chief Engineer's View of the NASA X-43A Scramjet Flight Test," Tech. Rep. AIAA 2005-3332, NASA Dryden Flight Research Center and NASA Langley Research Center, May 2005. AIAA/CIRA 13th International Space Planes and Hypersonic Systems and Technologies Conference, Capua, Italy. Available: `https://ntrs.nasa.gov/api/citations/20050175770/downloads/20050175770.pdf`.

[3] Liu, X., Wang, M., Liu, J., Ren, X., and Zhang, X., "Review and prospect of research on scramjet," *Acta Aeronautica et Astronautica Sinica*, Vol. 45, No. 5, 2024, p. 529878. https://doi.org/10.7527/S1000-6893.2023.29878.

[4] Fry, R. S., "A Century of Ramjet Propulsion Technology Evolution," *Journal of Propulsion and Power*, Vol. 20, No. 1, 2004, pp. 27–58. https://doi.org/10.2514/1.9178.

[5] Kuropatwa, M., Wegrzyn, N., and Kozuba, J., "Turbofan engines efficiency, historical trends, and future prediction - A review," *Safety & Defense*, Vol. 8, No. 2, 2022, pp. 82–90. https://doi.org/10.37105/sd.186.

[6] Del Gatto, D., Adamidis, S., Mourouzidis, C., and Brown, S., "Comparison of Alternative Engine Architectures for Next Generation Supersonic Aircraft," *Engineering Proceedings*, Vol. 90, No. 115, 2025. https://doi.org/10.3390/engproc2025090115, presented at the 14th EASN International Conference, Thessaloniki, Greece, 8-11 October 2024. Funded by EU Horizon 2020 SENECA project, grant No. 101006742.

[7] Riegler, C., and Bichlmaier, C., "The Geared Turbofan Technology - Opportunities, Challenges and Readiness Status," *1st CEAS European Air and Space Conference*, MTU Aero Engines GmbH, Munich, Germany, 2007.

[8] Huang, W., Yan, L., and Tan, J.-g., "Survey on the mode transition technique in combined cycle propulsion systems," *Aerospace Science and Technology*, Vol. 39, 2014, pp. 685–691. https://doi.org/10.1016/j.ast.2014.07.006.

[9] Yuan, H., Liu, J., Zhang, J., and Wang, Y., "The design and validation of over/under turbine-based combined cycle inlet," *Aerospace Science and Technology*, Vol. 105, 2020, p. 105960. https://doi.org/10.1016/j.ast.2020.105960.

[10] Saunders, J. D., Stueber, T. J., Thomas, S. R., Suder, K. L., Weir, L. J., and Sanders, B. W., "Testing of the NASA Hypersonics Project's Combined Cycle Engine Large Scale Inlet Mode Transition Experiment (CCE LIMX)," Tech. Rep. NASA/TM–2012-217217, NASA Glenn Research Center, Cleveland, Ohio, January 2012.

[11] PEI, X., WANG, B., QI, C., QIAN, Q., XIE, Q., LI, Z., and WANG, X., "Research progress in mode transition technologies for turbine-based combined cycle engines," *Journal of Tsinghua University (Science and Technology)*, Vol. 65, No. 12, 2025, pp. 2410–2448. https://doi.org/10.16511/j.cnki.qhdxxb.2026.26.008, URL https://www.sciopen.com/article/10.16511/j.cnki.qhdxxb.2026.26.008, publishing language: Chinese; abstract in English.

[12] Thomas, S. R., Perkins, H. D., and Trefny, C. J., "Evaluation of an Ejector Ramjet Based Propulsion System for Air-Breathing Hypersonic Flight," Tech. Rep. NASA TM-107422, NASA Lewis Research Center, Cleveland, Ohio, 1997. URL https://ntrs.nasa.gov/api/citations/19970017381/downloads/19970017381.pdf.

[13] Zhou, R., Wu, D., and Wang, J., "Progress of continuously rotating detonation engines," *Chinese Journal of Aeronautics*, Vol. 29, No. 1, 2016, pp. 15–29. https://doi.org/10.1016/j.cja.2015.12.006.

[14] Braun, E. M., Lu, F. K., Wilson, D. R., and Camberos, J. A., "Airbreathing rotating detonation wave engine cycle analysis," *Aerospace Science and Technology*, Vol. 27, No. 1, 2013, pp. 201–208. https://doi.org/10.1016/j.ast.2012.08.010.

[15] Wang, G., Liu, W., Liu, S., Zhang, H., Peng, H., and Zhou, Y., "Experimental verification of cylindrical air-breathing continuous rotating detonation engine fueled by non-premixed ethylene," *Acta Astronautica*, Vol. 189, 2021, pp. 722–732. https://doi.org/10.1016/j.actaastro.2021.09.009.

[16] Meng, H., Xiao, Q., Feng, W., Wu, M., Han, X., Wang, F., Weng, C., and Zheng, Q., "Air-breathing rotating detonation fueled by liquid kerosene in cavity-based annular combustor," *Aerospace Science and Technology*, Vol. 122, 2022, p. 107407. https://doi.org/10.1016/j.ast.2022.107407.

[17] Jourdaine, N., Tsuboi, N., Ozawa, K., Kojima, T., and Hayashi, A. K., "Three-dimensional numerical thrust performance analysis of hydrogen fuel mixture rotating detonation engine with aerospike nozzle," *Proceedings of the Combustion Institute*, Vol. 37, No. 3, 2019, pp. 3443–3451. https://doi.org/10.1016/j.proci.2018.09.024.

[18] Zheng, H., Meng, Q., Zhao, N., Li, Z., and Deng, F., "Numerical investigation on H_2/Air non-premixed rotating detonation engine under different equivalence ratios," *International Journal of Hydrogen Energy*, Vol. 45, No. 4, 2020, pp. 2289–2307. https://doi.org/10.1016/j.ijhydene.2019.11.014.

[19] Smirnov, N. N., Nikitin, V. F., Stamov, L. I., Mikhalchenko, E. V., and Tyurenkova, V. V., "Rotating detonation in a ramjet engine three-dimensional modeling," *Aerospace Science and Technology*, Vol. 81, 2018, pp. 213–224. https://doi.org/10.1016/j.ast.2018.08.003.

[20] Hou, Y., Cheng, M., Sheng, Z., and Wang, J., "Unsteady conjugate heat transfer simulation of wall heat loads for rotating detonation combustor," *International Journal of Heat and Mass Transfer*, Vol. 221, 2024, p. 125081. https://doi.org/10.1016/j.ijheatmasstransfer.2023.125081.

[21] Wu, Q., Lin, Z., Huang, X., and Zhang, D., "Flow characteristics and stability of induced shock waves in the isolator of rotating detonation ramjet under flight Mach number 2.5 conditions," *Aerospace Science and Technology*, Vol. 133, 2023, p. 108092. https://doi.org/10.1016/j.ast.2022.108092.

[22] Stechmann, D., Lim, D., and Heister, S. D., "Experimental Study of a High Pressure Rotating Detonation Wave Combustor for Rocket Applications," *6th European Conference for Aerospace Sciences*, 2015.

[23] Zhao, M., Zhang, L., Huo, W., Yang, H., and Yuan, Y., "Performance analysis of a rotating detonation model for future thermal power system using hydrogen as fuel," *Energy Reports*, Vol. 8, 2022, pp. 66–74. https://doi.org/10.1016/j.egyr.2021.11.036.

[24] Ji, Z., Zhang, H., and Wang, B., "Thermodynamic performance analysis of the rotating detonative airbreathing combined cycle engine," *Aerospace Science and Technology*, Vol. 113, 2021, p. 106694. https://doi.org/10.1016/j.ast.2021.106694.

[25] Liu, X.-Y., Cheng, M., Zhang, Y.-Z., and Wang, J.-P., "Design and optimization of aerospike nozzle for rotating detonation engine," *Aerospace Science and Technology*, Vol. 120, 2022, p. 107300. https://doi.org/10.1016/j.ast.2021.107300.

[26] Shapiro, A. H., *The Dynamics and Thermodynamics of Compressible Fluid Flow*, Vol. 1, Ronald Press, 1953.

[27] Anderson, J. D., *Modern Compressible Flow: With Historical Perspective*, 3rd ed., McGraw-Hill, 2003.

[28] Powers, J. M., *Mechanics of Fluids*, Cambridge University Press, 2023.

[29] Adler, B., *Aerospace Engineering Foundations: Hypersonic Aerodynamics and Aerothermodynamics*, Amazon, 2025.

[30] Oswatitsch, K., "Pressure Recovery for Missiles with Reaction Propulsion at High Supersonic Speeds (The Efficiency of Shock Diffusers)," Tech. Rep. NACA TM 1140, National Advisory Committee for Aeronautics, 1947. Translated from the original German report.

[31] Kantrowitz, A., and Donaldson, C. d., "Preliminary Investigation of Supersonic Diffusers," Tech. Rep. NACA-ACR-L5D20, National Advisory Committee for Aeronautics, May 1945.

[32] Fickett, W., and Davis, W. C., *Detonation: Theory and Experiment*, University of California Press, Berkeley, CA, 1979.

[33] Stodola, A., *Steam and Gas Turbines*, McGraw-Hill, New York, 1927.

[34] Qiu, X., Mallikarachchi, C., and Anderson, M., "A New Slip Factor Model for Axial and Radial Impellers," *ASME Turbo Expo 2007: Power for Land, Sea, and Air*, ASME, 2007. https://doi.org/10.1115/GT2007-27064, unified slip factor model for axial, radial, and mixed-flow impellers at design and off-design conditions.

[35] National Oceanic and Atmospheric Administration (NOAA), National Aeronautics and Space Administration (NASA), and U.S. Air Force, "U.S. Standard Atmosphere, 1976," Tech. Rep. NOAA-S/T 76-1562, U.S. Government Printing Office, Washington, DC, 1976. URL https://www.ngdc.noaa.gov/stp/space-weather/online-publications/miscellaneous/us-standard-atmosphere-1976/us-standard-atmosphere_st76-1562_noaa.pdf.